



A plastic constitutive equation incorporating strain, strain-rate, and temperature

Ji Hyun Sung^a, Ji Hoon Kim^b, R.H. Wagoner^{c,*}

^a Department of Mechanical Engineering, The Ohio State University, 2041 College Road, Columbus, OH 43210, USA

^b Materials Deformation Group, Korea Institute of Materials Science, 531 Changwondaero, Changwon, Gyeongnam 641-831, South Korea

^c Department of Materials Science and Engineering, The Ohio State University, 2041 College Road, Columbus, OH 43210, USA

ARTICLE INFO

Article history:

Received 24 November 2009

Received in final revised form 12 February 2010

Available online 15 March 2010

Keywords:

Constitutive equation

Work hardening

Dual-phase (DP) steel

Thermal–mechanical FE simulation

Deformation-induced heating

ABSTRACT

An empirical plasticity constitutive form describing the flow stress as a function of strain, strain-rate, and temperature has been developed, fit to data for three dual-phase (DP) steels, and compared with independent experiments outside of the fit domain. Dubbed the “H/V model” (for “Hollomon/Voce”), the function consists of three multiplicative functions describing (a) strain hardening, (b) strain-rate sensitivity, and (c) temperature sensitivity. Neither the multiplicative structure nor the choice of functions (b) or (c) is novel. The strain hardening function, (a), has two novel features: (1) it incorporates a linear combination coefficient, α , that allows representation of Hollomon (power law) behavior ($\alpha = 1$), Voce (saturation) behavior ($\alpha = 0$) or any intermediate case ($0 < \alpha < 1$), and (2) it allows incorporation of the temperature sensitivity of strain hardening rate in a natural way by allowing α to vary with temperature (in the simplest case, linearly). This form therefore allows a natural transition from unbounded strain hardening at low temperatures toward saturation behavior at higher temperatures, consistent with many observations. Hollomon, Voce, H/V models and others selected as representative from the literature were fit for DP590, DP780, and DP980 steels by least-squares using a series of tensile tests up to the uniform strain conducted over a range of temperatures. Jump-rate tests were used to probe strain rate sensitivity. The selected laws were then used with coupled thermo-mechanical finite element (FE) modeling to predict behavior for tests outside the fit range: non-isothermal tensile tests beyond the uniform strain at room temperatures, isothermal tensile tests beyond the uniform strain at several temperatures and hydraulic bulge tests at room temperature. The agreement was best for the H/V model, which captured strain hardening at high strain accurately as well as the variation of strain hardening with temperature. The agreement of FE predictions up to the tensile failure strain illustrates the critical role of deformation-induced heating in high-strength/high ductility alloys, the importance of having a constitutive model that is accurate at large strains, and the implication that damage and void growth are unlikely to be determinant factors in the tensile failure of these alloys. The new constitutive model may have application for a wide range of alloys beyond DP steels, and it may be extended to larger strain rate and temperature ranges using alternate forms of strain rate sensitivity and thermal softening appearing in the literature.

© 2010 Elsevier Ltd. All rights reserved.

* Corresponding author. Tel.: +1 614 292 2079; fax: +1 614 292 6530.

E-mail address: wagoner.2@osu.edu (R.H. Wagoner).

1. Introduction

Advanced high strength steels (AHSS) provide remarkable combinations of strength and ductility by careful control of microstructure of ferrite, martensite, and retained austenite components. Dual-phase (DP) steel microstructures consist of large islands (of approximately the grain size) of hard martensite embedded in a softer ferrite matrix, thus mimicking a typical discontinuous composite structure. DP steels are well-established but their widespread adoption has been limited because die tryouts show that forming failures can occur much earlier than predicted using standard forming limit diagrams (FLD) and commercial finite element (FE) programs. Unlike failures observed with traditional steels, unexpected DP steel failures occur in long channel regions of low R/t (bending radius/sheet thickness) as the sheet is drawn over the die radius while being stretched, bent and straightened. Such failures are often dubbed “shear fracture” by industrial practitioners (Huang et al., 2008; Sklad, 2008; Chen et al., 2009). Conventional wisdom has attributed this phenomenon to a special damage/void growth mechanism, possibly related to the large, hard martensite islands (Takuda et al., 1999; Horstemeyer et al., 2000; Lee et al., 2004; Sarwar et al., 2006; Wagoner, 2006; Vernerey et al., 2007; McVeigh and Liu, 2008; Xue, 2008; Sun et al., 2009).

Recent work was conducted by the authors to determine whether such unpredicted forming failures are a result of typical plastic localization or a special kind of fracture. Draw-bend tests which reproduce the conditions that promote “shear failure” were found to exhibit greatly varying formability depending on the strain rate in the test (Wagoner et al., 2009a,b). Furthermore, temperatures of up to 100 °C in sheet regions away from the necking area were measured, much higher than with typical traditional steels with lower strength/ductility combinations. It became apparent that the role of temperature in the flow stress, almost universally ignored in standard sheet forming simulations and mechanical property determinations, might be a critical factor. In order to consider these effects quantitatively, a reliable constitutive equation was needed in the range of strain, strain rate, and temperature encountered in such tests and forming operations.

1.1. Role of deformation-induced heating in plastic localization

Unlike the uniformly elevated temperature imposed in a warm forming process (usually applied to increase the inherent ductility of the alloy), the heat caused by plastic deformation in a local region of high strain has a detrimental effect on mechanical formability because most alloys soften with increasing temperature, and the softening occurs at the eventual fracture location (Kleemola and Ranta-Eskola, 1979; Ayres, 1985; Lin and Wagoner, 1986; Gao and Wagoner, 1987; Lin and Wagoner, 1987; Wagoner et al., 1990; Ohwue et al., 1992). The phenomenon can be seen as a kind of “reverse strain-rate sensitivity,” because the higher strain rate in an incipient or developed neck tends to increase the flow stress via strain-rate sensitivity (and thus delay failure) but also tends to decrease the flow stress via the material’s temperature sensitivity (thus promoting earlier failure) (Wagoner and Chenot, 1997; Ghosh, 2006).

The deformation-induced thermal effects are important at strain rates high enough that heat transfer out of the neck region is limited. At sufficiently low rates the deformation becomes quasi-isothermal and temperature sensitivity has a negligible effect. At sufficiently high rates the deformation is quasi-adiabatic and the heat stays where it is generated. Typical sheet-forming strain rates in the automotive industry are approximately 10/s (Fekete, 2009), which is close to the adiabatic limit for typical steels. Therefore, the role of temperature sensitivity of flow stress may be important if it is sufficiently high and the work of deformation (related to flow stress times ductility) is sufficient to raise the temperature significantly. For DP steels with high strength and ductility, an accurate description of flow stress incorporating temperature may be essential. Such a description, if verified, may also be useful for a large range of other materials and applications.

1.2. Plastic constitutive equations

The number, range and complexity of plastic constitutive equations proposed for metals are formidable. They take many forms, depending on application and intent. The application of interest in the current work is metal forming, sheet metal forming to be more precise. Typical sheet metal formability is related to the resistance to tensile necking, which is in turn related to the evolution of plastic flow stress in biaxial tensile stress states encountered during the progressive forming. Through-thickness stress is typically close to zero (i.e. plane stress) until failure is imminent.

Multi-axial aspects of the plastic constitutive response (yield surface shape, size, and location evolution) are often separated for convenience from one-dimensional (1-D) aspects that are obtainable from tensile tests carried out at various strain rates and temperatures. The current interest is in 1-D aspects. Since many material elements undergo strain paths close to proportional, strain reversal effects such as the Bauschinger effect can be ignored for many applications.

The preponderance of sheet metal forming is carried out at moderate strain rates (up to approximately 10/s (Fekete, 2009)) and nominally room temperature (although excursions of the order of up to 100 °C are possible because of heat generated deformation and friction during forming (Wagoner et al., 2009a,b)). For most sheet-formed metals of commercial interest (e.g. steel, aluminum, copper, titanium) under these conditions, strain hardening is the primary material factor resisting necking, with strain-rate and temperature sensitivity of flow stress being secondary.

As listed in Appendix A, there are integrated constitutive equations relating plastic flow stress with strain, strain rate, and temperature (which is the focus of the current work). The strain hardening representations (at constant strain rate and

temperature) are of two main types (Table 1): those that approach a saturation stress at large strain (e.g. Brown–Anand (“BA”) model (Anand, 1982, 1985; Brown et al., 1989), MTS model (Kocks, 1976; Mecking and Kocks, 1981; Follansbee and Kocks, 1988), Modified Bodner–Partom (“BP”) model (Bodner and Partom, 1975; Chen et al., 2008) and Lin–Wagoner (“LW”) Model (Lin and Wagoner, 1987)) and those that are unbounded at large strain (e.g. Zirilli–Armstrong (“ZA”) model (Zerilli and Ronald, 1987), Rusinek–Klepaczko (“RK”) model (Klepaczko, 1987; Rusinek and Klepaczko, 2001; Rusinek et al., 2007) and Khan–Huang–Liang (“KHL”) model (Khan and Huang, 1992; Khan and Liang, 1999; Khan and Zhang, 2000, 2001; Khan et al., 2004; Khan et al., 2007)). The first group may be called, in short, “saturation” or “Voce” models (Voce, 1948; Follansbee and Kocks, 1988) while the second may be called “Hollomon” or “power-law” models (Hollomon, 1945); the proper names refer to the simplest empirical versions of these strain hardening forms appearing in the literature, with three parameters or two parameters, respectively.

The saturation-type laws are typically found suitable for materials at higher homologous temperatures (and most face-centered cubic (FCC) metals such as aluminum and copper (Mishra et al., 1989; Choudhary et al., 2001) at room temperature) while power-law-type models are more suitable for body-centered cubic (BCC) metals and at low homologous temperatures. For example, iron alloys are known to continue strain hardening at strains up to at least 3 (Johnson and Holmquist, 1988).

Integrated constitutive equations may be subdivided in another way: those that accommodate strain hardening rate changes with temperature changes (e.g. BA model, MTS model, Modified BP model, LW Model and RK model) and those that do not (e.g. ZA model and KHL model), Table 1. As shown in Table 1, only the saturation-type integrated laws incorporate strain hardening rates that are sensitive to temperature (beyond fixed multiplicative or additive functions), with one exception: the RK model. The RK model (2001) incorporates power-law strain hardening with a power, n , that varies in a prescribed manner with temperature as shown in Appendix A. It is similar in concept to the LW model (1987), where strain hardening parameters in a saturation-like law are allowed to vary linearly with temperature, thus using six material parameters (Appendix A).

In addition to the integrated constitutive equations mentioned above, there are myriad ways to choose and combine otherwise independent basis functions of strain, strain rate and temperature, which may be generally represented as $f(\varepsilon)$, $g(\dot{\varepsilon})$, and $h(T)$, respectively, where ε is true tensile strain, $\dot{\varepsilon}$ is true strain rate, and T is temperature. (See Appendix B for a list of typical functions of this kind. The total number of multiplicative combinations for the choices presented there alone is 126.) The basis functions may be combined multiplicatively (Hutchison, 1963; Kleemola and Ranta-Eskola, 1979; Johnson and Cook, 1983; Lin and Wagoner, 1986), additively (Wagoner, 1981b; Ghosh, 2006), or by some combination (Zerilli and Ronald, 1987) thereof. Each material model of these types prescribes the strain hardening at each temperature as a simple multiple or addition (or combination), rather than allowing for the character or rate of strain hardening to vary with temperature, hence the definition adopted for Table 1 to decide whether strain hardening is a function of temperature or not. Common choices for the basis functions $f(\varepsilon)$, $g(\dot{\varepsilon})$, and $h(T)$, are presented in Appendix B. Several of these combinations have been reviewed and fit to tensile data in the literature (Lin and Wagoner, 1986).

1.3. Purpose of the current work

The purpose of the current work is to develop and verify an empirical plastic constitutive model that meets the following conditions while introducing the minimum number of undetermined parameters:

- (1) it reproduces strain hardening accurately at large strain from fitting in the uniform tensile range,
- (2) it captures both extreme kinds of strain hardening forms as well as intermediate cases: bounded (power law) and unbounded (saturation),
- (3) it captures the change of strain hardening character and rate depending on temperature, and
- (4) it is capable of predicting strain localization and failure under typical sheet forming conditions of strains, strain rates, and temperatures.

In order to accomplish these goals, a new multiplicative type phenomenological constitutive equation, the H/V model, is introduced. The H/V model is a linear combination of the Hollomon and Voce strain hardening equations with a tempera-

Table 1

Classification of integrated 1-D plastic constitutive equations that incorporate the effects of strain, strain-rate, and temperature.^a

	Unbounded-stress at large strain	Strain hardening change with temperature
Brown–Anand	N	Y
MTS	N	Y
Modified Bodner–Partom	N	Y
Lin–Wagoner	N	Y
Zirilli–Armstrong	Y	N
Khan–Huang–Liang	Y	N
Rusinek–Klepaczko	Y	Y

^a For the classification shown in Table 1, whenever the flow stresses for a given strain at two temperatures differ only by a constant ratio or difference, then the strain hardening rate is deemed not to depend on temperature.

ture-dependent proportion. The temperature-dependent proportion represents the change of strain hardening character and rate as temperature changes. Standard multiplicative forms for strain rate sensitivity and thermal softening are incorporated for fitting and testing. The initial application, the one for which testing is conducted, is for sheet metal forming at rates up to 10/s with deformation-induced heating to temperatures up to 100 deg. C. These are conditions normally encountered in nominally room-temperature pressforming operations; the application that inspired the current work. Nonetheless, the H/V model may have application outside of this regime with or without changes in forms to accommodate larger ranges of strain rate and temperature.

2. H/V constitutive equation

A new empirical work hardening constitutive model, H/V model, is proposed as three multiplicative functions, Eq. (1).

$$\sigma = \sigma(\varepsilon, \dot{\varepsilon}, T) = f(\varepsilon, T) \cdot g(\dot{\varepsilon}) \cdot h(T) \quad (1)$$

Functions f , g , and h together represent the effects of strain, strain rate, and temperature, respectively, on the tensile flow stress σ . g and h are chosen from any of several standard forms (see Appendix B), but the strain hardening function, f , is novel: it incorporates the temperature sensitivity of strain hardening rate via a linear combination of Voce (saturation) (1948) and Hollomon (power-law) (1945) strain-hardening forms.

2.1. Strain hardening function, $f(\varepsilon, T)$

The function $f(\varepsilon, T)$ represents the major departure and contribution of the new development. The motivation for the development of $f(\varepsilon, T)$ is illustrated in Fig. 1(a), which shows strain hardening curves for a dual-phase steel, DP 780, at three temperatures. To compare the strain hardening curve shapes, the stresses are normalized by dividing by the yield stresses at each temperature, Fig. 1(b). Clearly the strain hardening rate varies with temperature, being lower at higher temperatures. This behavior, which is seldom captured by existing constitutive models, is one of the two principal motivations for the current development.

In this study, a strain hardening function $f(\varepsilon, T)$ of the following form is proposed:

$$f(\varepsilon, T) = \alpha(T)f_H + (1 - \alpha(T)) \cdot f_V \quad (2)$$

$$\begin{cases} \alpha(T) = \alpha_1 - \alpha_2(T - T_0) \\ f_H = H_{HV}\varepsilon^{n_{HV}} \\ f_V = V_{HV}(1 - A_{HV}e^{-B_{HV}\varepsilon}) \end{cases} \quad (3)$$

where T_0 is a reference temperature (298 K for simplicity), and $\alpha_1, \alpha_2, H_{HV}, n_{HV}, V_{HV}, A_{HV}$, and B_{HV} are material constants. The function $\alpha(T)$ allows a more Voce-like curve at higher temperatures, and a more Hollomon-like curve at lower temperatures or vice versa, depending on the sign of α_1 . If $\alpha(T) = 1$, the H/V model becomes a pure Hollomon model and if $\alpha(T) = 0$ it becomes a pure Voce model. If an intermediate hardening rate is sought that does not depend on temperature, α may be chosen to be constant: $0 < \alpha_0 < 1$.

2.2. Strain rate sensitivity function $g(\dot{\varepsilon})$, temperature sensitivity function $h(T)$

The functions $g(\dot{\varepsilon})$ and $h(T)$ within the H/V model are not novel; the exact form may be selected from among those appearing in the literature, as listed in Appendix B, or as otherwise devised. It is anticipated that the choice of form of these functions will not be important over the range of strain rates (up to 10^{-1} /s) and temperatures (25–100 °C) encountered in the testing carried out in the current work. For extended ranges, the choice of $g(\dot{\varepsilon})$ and $h(T)$ may become more clear. The choices of terms $g(\dot{\varepsilon})$ and $h(T)$ for the implementation of the H/V model tested in the current work will be explained in more detail in Section 4.1.

3. Experimental procedures

The experiments were chosen to correspond to typical sheet forming practice applied to three DP steels representing a range of strengths typical of automotive body applications. Constitutive models were fit using standard tensile tests up to the uniform strain. The quality of the fits was then probed using tensile tests and hydraulic bulge tests to failure.

3.1. Materials

DP steels exhibit good formability and high strength derived from a microstructure that is a combination of a soft ferrite matrix and a hard martensite phase “islands.” Three grades of DP steels of nominally 1.4 mm thickness, DP590, DP780, and DP980, were provided by various suppliers, who requested not to be identified. DP590 was supplied without coating, DP780 with hot-dipped galvanized coating (HDGI), and DP980 with hot-dipped galvaneal coating (HDGA). The chemical

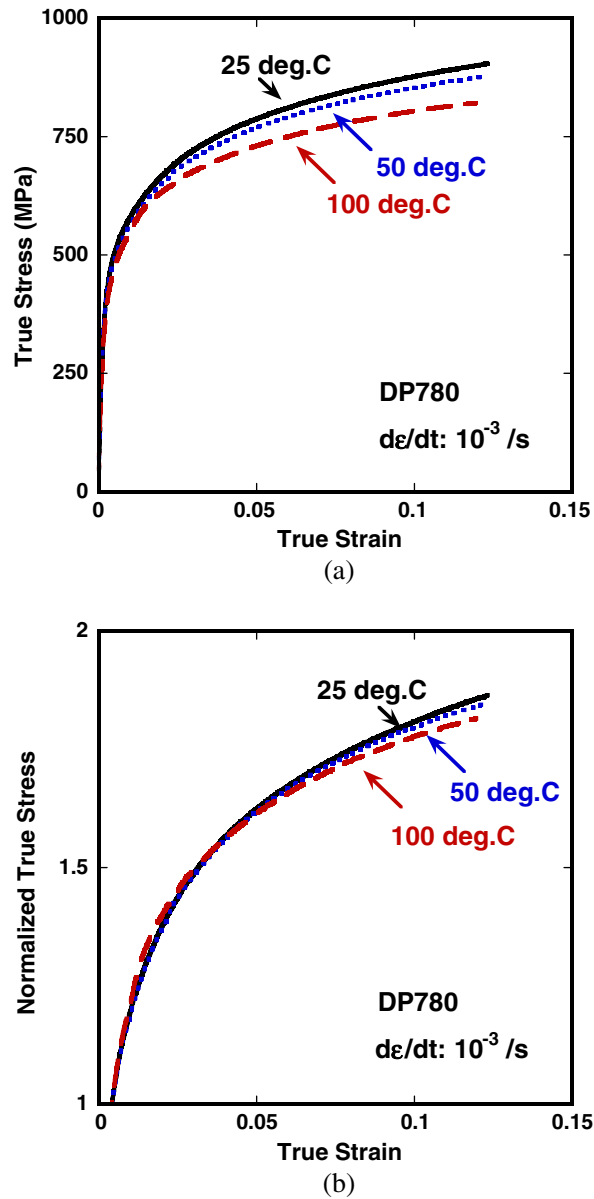


Fig. 1. Stress–strain response of DP780 at three temperatures: (a) experimental curves and (b) the same data, replotted with the stress divided by the initial yield stress to reveal strain-hardening differences.

compositions were determined utilizing a Baird OneSpark Optical Emission Spectrometer (HVS-OES) based on ASTM E415-99a(05) and standard tensile tests were carried out according to ASTM E8-08 at a crosshead speed of 5 mm/min. Both kinds of tests were conducted at General Motors North America (GMNA, 2007). The chemical compositions and standard ASTM standard tensile properties appear in Tables 2 and 3, respectively. In order to distinguish normal anisotropies measured from sheets of the original thickness and those thinned for balanced biaxial testing (as will be discussed in Section 3.5), symbols r_1 and r_2 in Table 3 refer to sheets of original thickness and thinned thickness, respectively.

Table 2
Chemical composition of dual-phase steels in weight percent (balance Fe).^a

	C	Mn	P	S	Si	Cr	Al	Ni	Mo	Nb	Ti	V	B
DP590	0.08	0.85	0.009	0.007	0.28	0.01	0.02	0.01	<.01	<.002	<.002	<.002	<.0002
DP780	0.12	2.0	0.020	0.003	0.04	0.25	0.04	<.01	0.17	<.003	<.003	<.003	<.0002
DP980	0.10	2.2	0.008	0.002	0.05	0.24	0.04	0.02	0.35	<.002	<.002	<.002	<.0002

^a Chemical analysis was conducted at General Motors North America (GMNA, 2007).

Table 3
Mechanical properties of dual-phase steels.^a

	Thickness (mm)	0.2% YS (MPa)	UTS (MPa)	e_u (%)	e_t (%)	n^b	Δr^c	r_1^c	r_2^d	a^d
DP590	1.4	352	605	15.9	23.2	0.21	0.30	0.84	0.98	1.83
DP780	1.4	499	815	12.7	17.9	0.19	-0.11	0.97	0.84	1.86
DP980	1.4	551	1022	9.9	13.3	0.15	-0.23	0.76	0.93	1.90

^a Tests were conducted at General Motors North America (GMNA, 2007) with 5 mm/min crosshead speed at room temp except for test of r_2 and a which were conducted at Alcoa (ATC, 2008; Brem, 2008) with thinned materials.

^b n value was calculated from an engineering strain interval of 4–6%.

^c Δr and r_1 were calculated at the uniform strain of original thickness material using $\Delta r = (r_0 - 2r_{45} + r_{90})/2$ and $r = (r_0 + 2r_{45} + r_{90})/4$, respectively.

^d r_2 value was calculated at the uniform strain of thinned materials using $r = (r_0 + 2r_{45} + r_{90})/4$ and a was found by the fit of bulge test result to tensile test data (using Eq. (9)) considering anisotropy (r_2) of thinned materials.

3.2. Material variation

In order to assure uniform, reproducible material properties in this work, a study was undertaken to determine variations of mechanical properties across the width of a coil. DP steels can exhibit more significant variations in this regard (as compared with traditional mild or HSLA steels) because of the complex thermo-mechanical treatment they undergo during production, Fig. 2. The standard deviation of the ultimate tensile stress for DP590 was 25 MPa, a scatter greater than 4% of the average UTS.

In order to quantify the spatial distribution of material properties and with a goal to minimize such effects on subsequent testing, numerous rolling direction (RD) tensile tests were conducted with simplified rectangular (non-shouldered) tensile specimens of DP590 having gage regions between the grips of 125 mm \times 20 mm. (As will be shown later, see Fig. 4, use of the rectangular specimens introduces no significant errors up to the uniform elongation.) In order to minimize the effect of sheared edge quality, the specimen edges were smoothed with 120 grit emery cloth (a practice that was followed for all tensile tests used in this work). The results from these specimens are summarized in Fig. 3: specimens within 360 mm of the coil edge (and thus more than 390 mm from the coil center line) exhibit systematic and significant variations in thickness and UTS, while those in the central region do not. A similar set of tests was performed for a DP980 steel (not the one used elsewhere in the current work) with the coil width of 1500 mm. The central region more than 300 mm from the edges had uniform properties. For the three materials used in the current work, DP590 (coil width 1500 mm), DP780 (coil width 1360 mm), DP980 (coil width 1220 mm), only material at least 360 mm from the coil edges was used.

3.3. Tensile testing

ASTM E8–08 sheet tensile specimens with 0% and 1% width taper were initially used for tensile testing, but failures occurred frequently outside of the gage region, thus making the consistent measurement of total elongation problematic. The failures outside of the gage region were more prevalent at elevated temperatures. In order to obtain consistent test results, the width taper was increased to 2%, which proved sufficient to insure failure at the center of the specimen for all tests. As expected (Raghavan and Wagoner, 1987), the increased taper reduced the total elongation, but there was no significant effect on stress–strain measurement up to the uniform elongation, Fig. 4.

The consistency and reproducibility of tensile results after these two improvements, that is, using material from the center of the coil and specimens with 2% width tapers, are illustrated in Fig. 5. The standard variation of UTS is less than 2 MPa

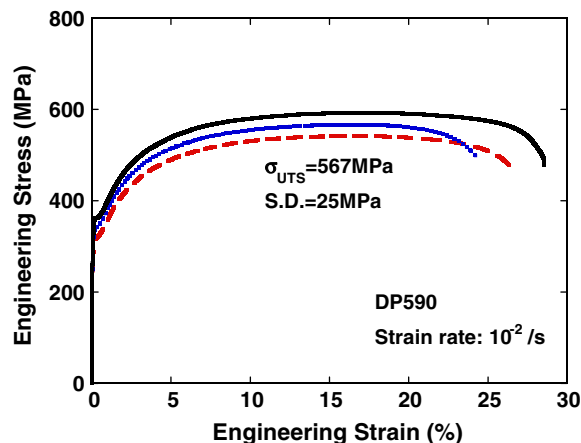


Fig. 2. Typical range of tensile behavior for DP590 steel specimens selected from various positions across the width of a coil.

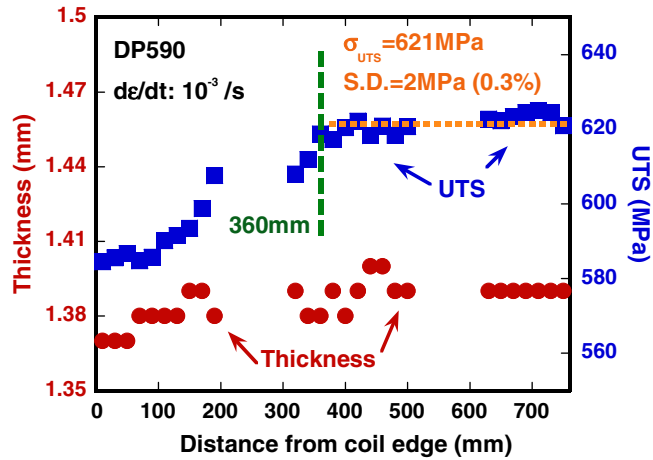


Fig. 3. Variation of sheet thickness and ultimate tensile strength with position from the edge of a coil (coil width of 1500 mm).

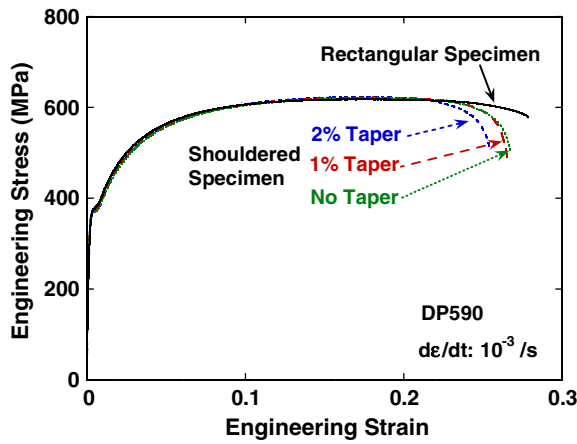


Fig. 4. Effect of tensile specimen geometry on measured stress–strain curves.

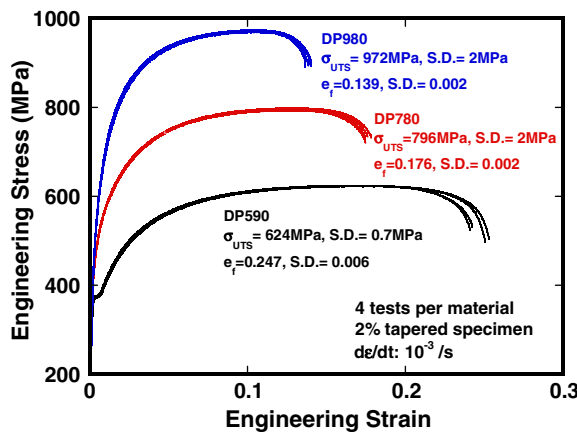


Fig. 5. Consistency and scatter of tensile results for three DP steels using 2% tapered tensile specimens and material at least 360 mm away from the edge of the coil.

(less than 0.3 % of the average value for each material), and the variation of the total elongation is less than 0.006 (less than 2.5% of the average value for each material). In view of these results, specimens with 2% tapers cut from the central region of the coil were used for all subsequent tensile testing.

For finding the parameters for the selected constitutive equations, isothermal tensile tests were conducted at 25 °C, 50 °C, and 100 °C using a special test fixture designed for tension–compression testing (Boger et al., 2005; Piao et al., 2009). In this application, the side plates that are pressed against the surface of the specimen (with a force of 2.24 kN) were not required to stabilize the specimen mechanically against buckling but served instead to heat the specimen for the 50 °C and 100 °C tests and to maintain near-isothermal conditions throughout the contact length and testing time for all tests. For strain rates up to 10^{-3} /s, the temperature measured in the gage length of the specimen using embedded thermocouples was maintained within 1 °C of the original one up to the uniform strain for all three materials. This method has several advantages compared with performing tensile tests in air in a furnace, including rapid heat-up (about 3 min to achieve 250 °C), uniform temperature along the length, and direct strain measurement using a laser extensometer.

The data was corrected for side plate friction (which was minimized using Teflon sheets) and the slight biaxial stress (which was about 1.5 MPa) using procedures presented elsewhere (Boger et al., 2005). The friction coefficient was determined from the slope of a least-squares line through the measured maximum force vs. four applied side forces (0, 1.12, 2.24 and 3.36 kN). The friction coefficients obtained in this way were 0.06, 0.05 and 0.06 for DP590, DP780 and DP980, respectively.

Examples of the tensile testing data at a strain of 10^{-3} /s illustrate the effect of test temperature on the stress–strain curves (Fig. 6), the yield and ultimate tensile stresses (Fig. 7), and the uniform and total elongations (Fig. 8). The reduced elongation to failure of higher temperatures is a direct consequence of the lower strain hardening.

For the purpose of comparison with FE simulation, non-isothermal tensile tests were also conducted at a strain rate of 10^{-3} /s in air at room temperature.

3.4. Strain rate jump tests

For materials with limited strain rate sensitivity relative to strength, even small differences of strength from specimen-to-specimen introduce large relative errors. Jump-rate tensile tests remove specimen-to-specimen variations and thus are preferred under these conditions. Strain rate jump-down tests, i.e. abruptly changing from a higher strain rate to lower strain rate, were employed in this study. (Stress–relaxation tests can also remove specimen variations but usually can only be used for very low strain rates, less than 10^{-6} /s (Wagoner, 1981b).) Fourteen down-jump rate changes, with one jump per tensile test (Saxena and Chatfield, 1976), were conducted at engineering strains of 0.1, 0.08, 0.06 for DP590, DP780, and DP980 steels, respectively, using the following pairs of rates: 0.5/s → 0.1/s, 0.5/s → 0.05/s, 0.1/s → 0.01/s, 0.1/s → 0.001/s, 0.05/s → 0.01/s, 0.05/s → 0.005/s, 0.01/s → 0.001/s, 0.001/s → 0.0001/s. The jumps 0.1/s → 0.01/s, 0.01/s → 0.001/s and 0.001/s → 0.0001/s were repeated three times. It has been shown that strain rate sensitivity is nearly independent of strain for steels (Wagoner, 1981a), which makes jump tests at a single intermediate strain sufficient.

For each down jump, a logarithmic strain rate sensitivity value was determined from the flow stresses σ_1 and σ_2 at the two strain rates $\dot{\epsilon}_1$ and $\dot{\epsilon}_2$, respectively, for an average strain rate of the two tested strain rates as shown:

$$\frac{\sigma_2}{\sigma_1} = \left(\frac{\dot{\epsilon}_2}{\dot{\epsilon}_1} \right)^m \rightarrow m = \frac{\ln(\sigma_2/\sigma_1)}{\ln(\dot{\epsilon}_2/\dot{\epsilon}_1)} \quad (4)$$

$$\dot{\epsilon}_{average} = \sqrt{\dot{\epsilon}_1 \dot{\epsilon}_2} \quad (5)$$

The stress after the jump shows a transient response that can be minimized by extrapolating both the higher rate curve and the lower rate curve to a common true strain 0.005 beyond the jump strain, at which point σ_1 and σ_2 are found (Wagoner, 1981a). The procedure is illustrated in Fig. 9 for the case of DP590 with a jump from 10^{-1} /s to 10^{-2} /s. The response at the higher first strain rate over a true strain range of 0.02 is fit to a fourth-order polynomial and extrapolated to the common

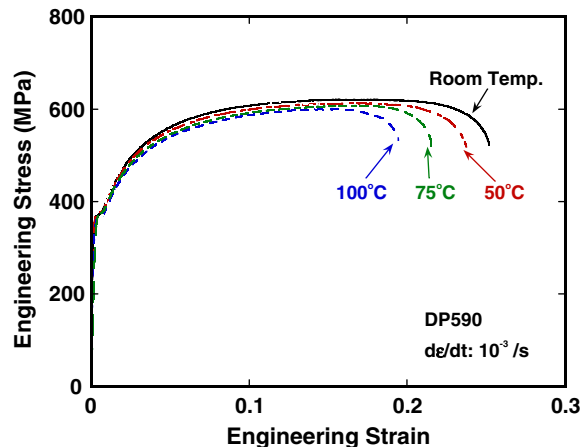


Fig. 6. Variation of strain hardening and failure elongation of DP590 with test temperature.

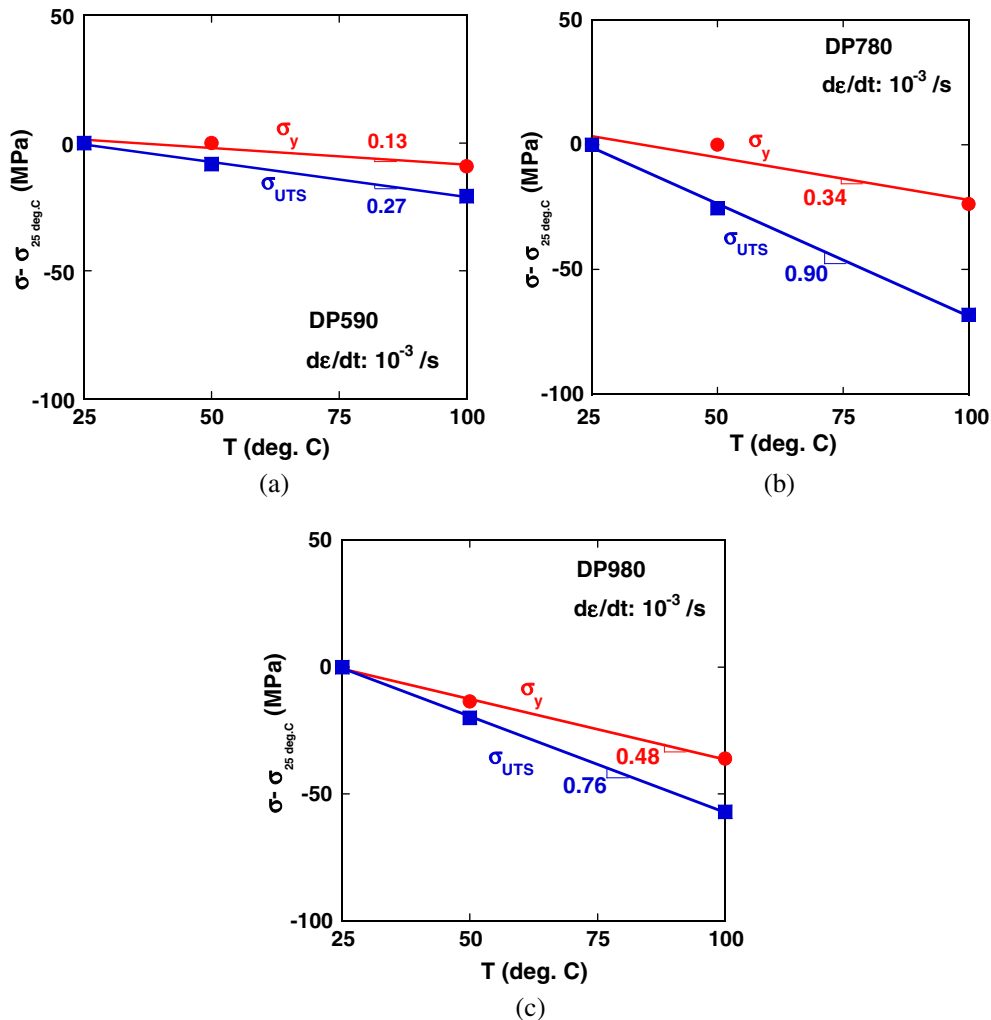


Fig. 7. Variation of yield stress and ultimate tensile stress with test temperature: (a) DP590, (b) DP780 and (c) DP980.

strain. The response at the second lower strain rate is similarly fit to a strain range of 0.02 starting at a true strain 0.01 higher than the jump strain, and is extrapolated to the common strain. The stresses from these extrapolated curves at the common strain are used to determine the m value from Eq. (4).

3.5. Hydraulic bulge tests

Hydraulic bulge tests were conducted at the Alcoa (ATC, 2008). Because of force limits of the ATC hydraulic bulge test system, the materials were machined from one side, from an as-received thickness of 1.4 mm–0.5 mm. The stress–strain response of thinned materials was within standard deviations of 5–10 MPa of the original thickness materials depending on the material. The die opening diameter was 150 mm and the die profile radius was 25.4 mm. For materials that exhibit in-plane anisotropy, the stress state near the pole is balanced biaxial tension (Kular and Hillier, 1972) with through-thickness stress negligible for small thickness/bulge diameter ratios (Ranta-Eskola, 1979). In-plane membrane stress, σ_b , and the magnitude of thickness strain, ϵ_t , are given by Eq. (6) and Eq. (7), respectively.

$$\sigma_b = \frac{pR}{2t} \quad (6)$$

$$\epsilon_t = 2 \ln \left(\frac{D}{D_0} \right) \quad (7)$$

where p is pressure, R is a radius of bulge, t is current thickness, D is current length of extensometer, and D_0 is the initial length of the extensometer, 25.4 mm. The radius of curvature R , is measured using a spherometer with each leg located at a fixed distance of 21.6 mm from the pole. More detailed information for the Alcoa testing machine has appeared elsewhere (Young et al., 1981).

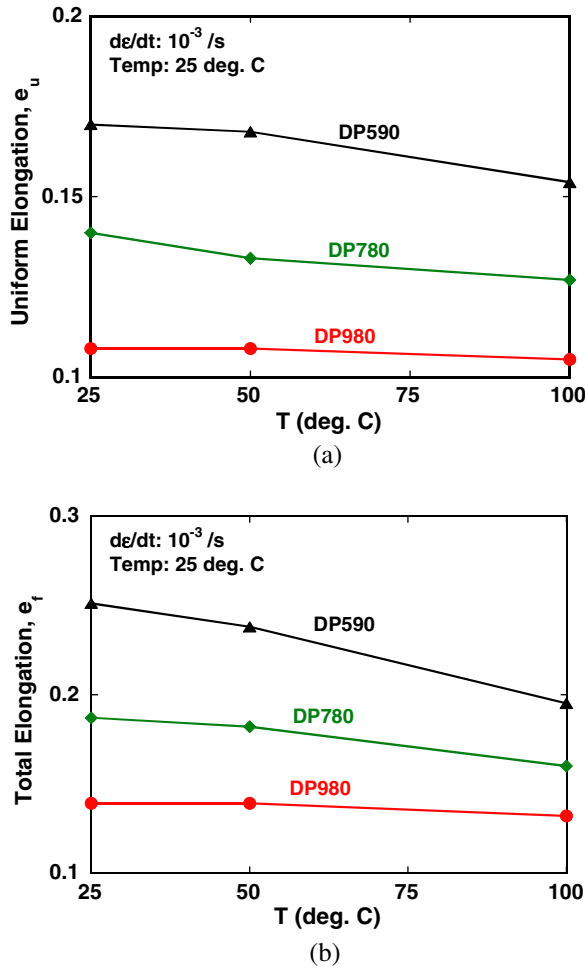


Fig. 8. Ductility change with temperature: (a) uniform elongation (e_u) and (b) total elongation (e_t).

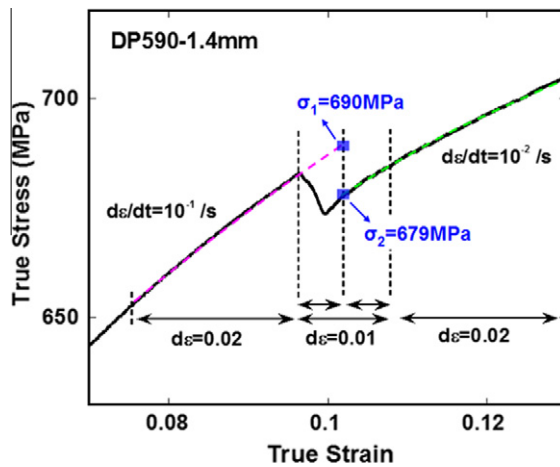


Fig. 9. Schematic illustrating the procedure for calculating of the strain rate sensitivity, m , for a down jump from 10^{-1} /s to 10^{-2} /s, for DP590 at an engineering strain of 0.1 (true strain of 0.095).

For an isotropic material, the von Mises effective stress and strain are equal to σ_b and ϵ_t , respectively. Because the DP steels tested here exhibit normal anisotropy, corrections were made for the known normal anisotropy parameters, r_2 (the normal anisotropy was measured using thinned samples at the uniform strain), shown in Table 3 and best-fit values of the material parameter anisotropy parameter a corresponding to the Hill 1979 non-quadratic yield function (Hill, 1979):

$$2(1 + r_2)\bar{\sigma}^a = (1 + 2r_2)|\sigma_1 - \sigma_2|^a + |\sigma_1 + \sigma_2|^a \quad (8)$$

The equations for obtaining the appropriate tensile effective stresses and strains for a balanced biaxial stress state have been presented (Wagoner, 1980):

$$\bar{\sigma} = \frac{2\sigma_1}{[2(1 + r_2)]^{1/a}}, \quad \bar{\varepsilon} = \varepsilon_1[2(1 + r_2)]^{1/a} \quad (9)$$

where ε_1 is half of the absolute value of the thickness strain. The value of a was found for each material using Eq. (9) and equating the effective stress and strain from a tensile test and bulge test at an effective strain equal to the true uniform strain in tension for each material, Table 3.

3.6. Coupled thermo-mechanical finite element procedures

The proposed constitutive equation was tested using a thermo-mechanical FE model of a tensile test with the same specimen geometry as in the experiments. ABAQUS Standard Version 6.7 (ABAQUS, 2007) was utilized for this analysis. One half of the physical specimen is shown in Fig. 10 with thermal transfer coefficients, but only one-quarter of the specimen was modeled, as reduced by mirror symmetry in the Y and Z directions. Eight-noded solid elements (C3D8RT) were used for coupled temperature-displacement simulations with two element layers through the thickness. The grip was modeled as a rigid body.

A von Mises yield function and the isotropic hardening law were adopted for simplicity in view of the nearly proportional uniaxial tensile stress path throughout most of the test and the normal anisotropy values near unity for the DP steels, Table

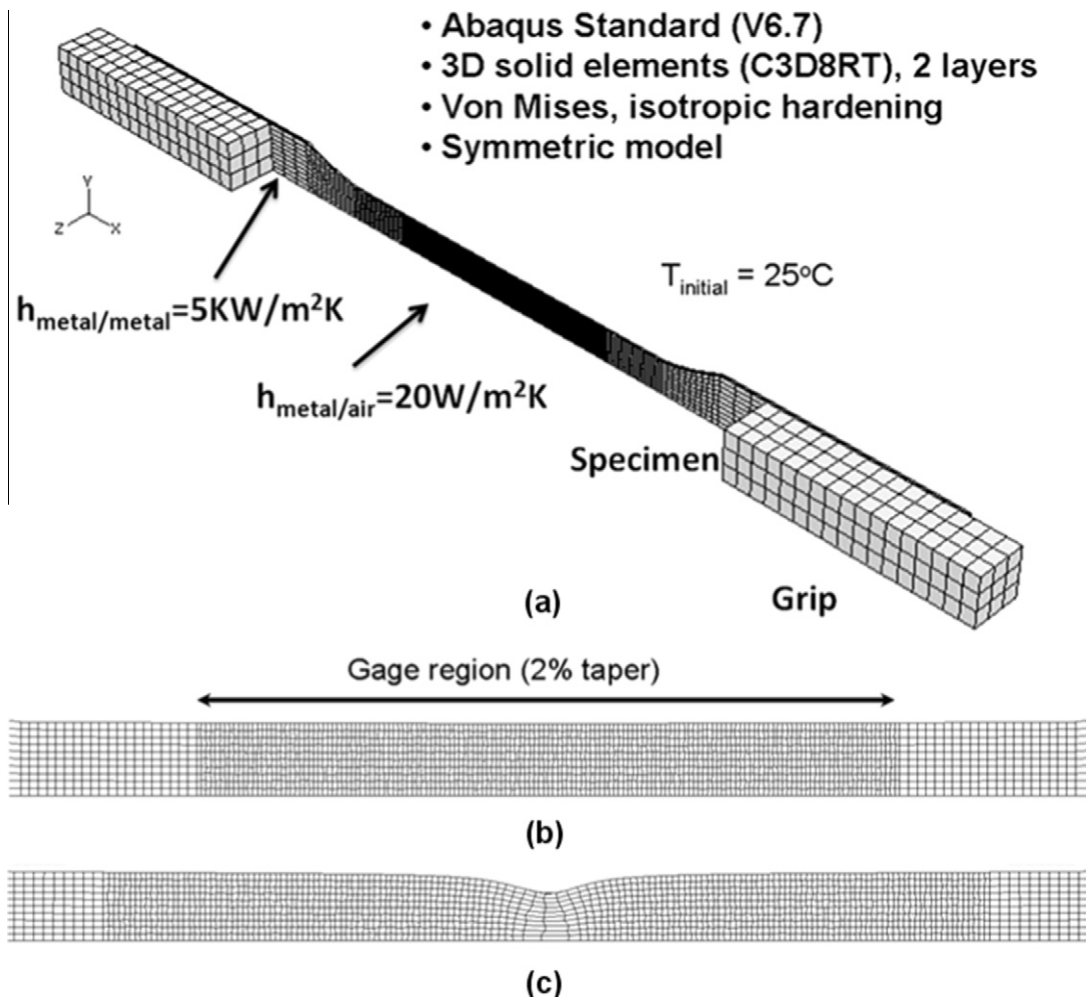


Fig. 10. FE model for tensile test: (a) schematic of the model with thermal transfer coefficients, (b) central region of the mesh before deformation and (c) central region of the mesh after deformation.

3. The 2% tapered specimen geometry required for experimental reproducibility automatically initiates plastic strain localization at the center of the specimen without introducing numerical defects for that purpose. The total elongation (ϵ_f) from each simulation was defined by the experimental load drop at failure. The simulation accuracy was evaluated based on the comparison of total elongation with experiments at this same load.

3.7. Determination of thermal constants

For thermal–mechanical FE simulation, various thermal constants are required. The following constants were determined using JMatPro (Sente-Software, 2007) based on chemical composition: thermal expansion coefficient: linear variation from $1.54 \times 10^{-6}/K$ at 25 °C to $1.58 \times 10^{-6}/K$ at 200 °C, heat capacity: linear variation from 0.45 J/gK at 25 °C to 0.52 J/gK at 200 °C, and thermal conductivity: piecewise linear variation of 36.7 W/m K at 25 °C, 36.9 W/m K at 70 °C, 36.8 W/m K at 100 °C and 36 W/m K at 200 °C. Heat transfer coefficient of metal–air contact was measured as 20W/m² K and heat transfer coefficient of metal–metal contact were taken from the literature as 5 KW/m² K (Burte et al., 1990).

A fraction of the plastic work done during deformation is converted to heat, with the remainder stored elastically as defects (Hosford and Caddell, 1983). The relationship between adiabatic temperature rise and plastic work is as follows:

$$\Delta T = \frac{\eta}{\rho C_p} \int \sigma d\epsilon_p \tag{10}$$

where η is a fraction of heat conversion from plastic deformation, ρ is density of the material and C_p is heat capacity at constant pressure. In order to measure η for DP steels, temperatures were recorded during tensile tests using three thermocouples that were capacitance discharge welded onto specimens on the longitudinal centerline at locations at the center and ± 5 mm from the center. The specimen was wrapped with glass fiber sheet to establish quasi-adiabatic conditions at a strain rate of $5 \times 10^{-2}/s$. Fig. 11 shows the results for DP590 and the acceptable correspondence to a value of 0.9 for the parameter η . η was measured only for DP590, but the value 0.9 was used for each of the three materials.

4. Results and discussion

4.1. Determination of best-fit constitutive constants

As shown by the experimental points shown in Fig. 12, the strain rate sensitivity index, m , is not independent of strain rate for any of the steels, so the power-law model (Eq. (B.8)) and Johnson–Cook rate law (Eq. (B.9)) were rejected as inadequate. The Wagoner rate law (Eq. (B.10)) and a simplified version the Wagoner law with a linear variation of m with logarithmic value of strain rate, Eq. (11) below, represent the data equally over this strain rate range as shown in Fig. 12, so the simpler law was selected:

$$\sigma = \sigma_{\dot{\epsilon}_0} \left(\frac{\dot{\epsilon}}{\dot{\epsilon}_0} \right)^{\gamma_2 + (\gamma_1/2) \log(\dot{\epsilon}/\dot{\epsilon}_0)} \tag{11}$$

where $\sigma_{\dot{\epsilon}_0}$ is a stress at $\dot{\epsilon}_0$ and γ_1 and γ_2 are material constants.

The linear variation law, Eq. (11), had slightly better correlation coefficients ($R^2 = 0.94$ – 0.99) than those for the Wagoner rate law ($R^2 = 0.82$ – 0.97). The best-fit values for the parameters for each model are shown in Table 4.

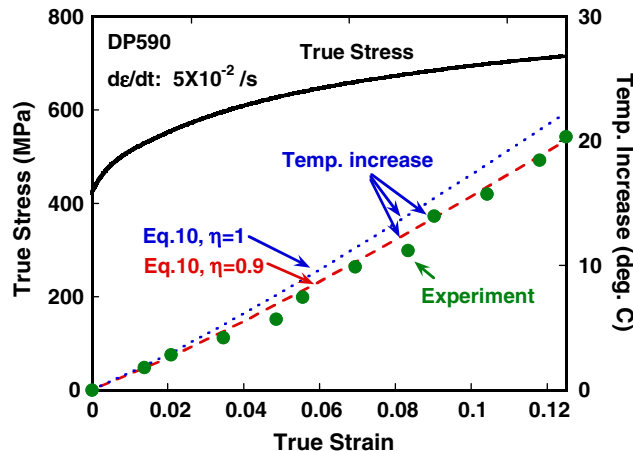


Fig. 11. Flow stress and temperature increase during a tensile test at a nominal strain rate of $5 \times 10^{-2}/s$, DP590.

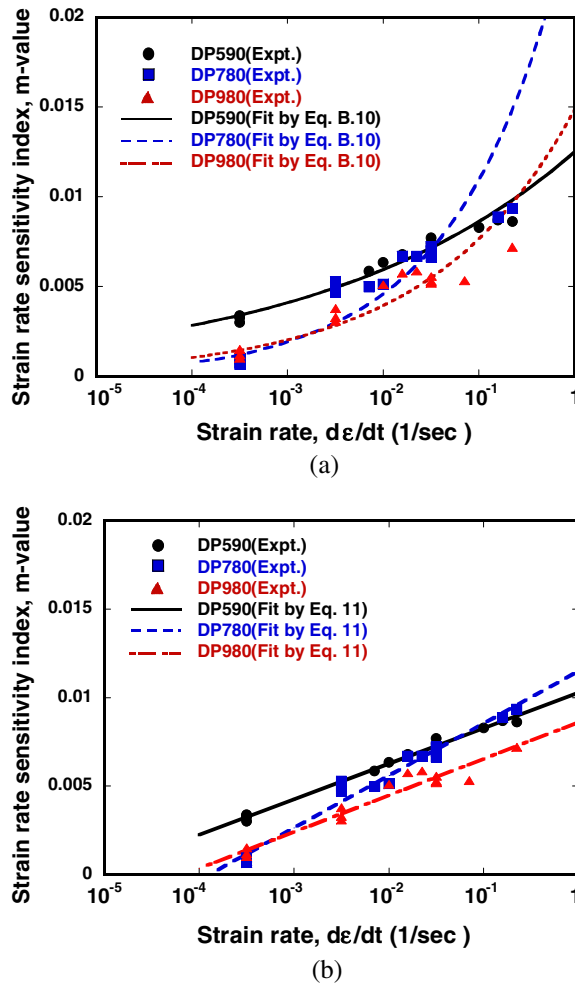


Fig. 12. Measured strain rate sensitivities, m , and their representation by strain rate sensitivity laws: (a) Wagoner rate law (Wagoner, 1981a) and (b) linearized version of Wagoner rate law.

Table 4
Parameters describing the strain rate sensitivity according to three laws.

	Power law (m_{avg})	Wagoner rate law		Linear law	
		m_l	m_0	γ_1	γ_2
DP590	0.0062	0.162	0.0125	0.0020	0.0103
DP780	0.0050	0.378	0.0263	0.0030	0.0115
DP980	0.0041	0.289	0.0148	0.0021	0.0086

The remainder of the H/V law was fit using results from continuous, isothermal tensile tests in the uniform strain range conducted at a strain of $10^{-3}/s$ and at three temperatures: 25, 50, and 100 °C, Fig. 13 (Note that the H/V model reproduces the variation of strain hardening rate in the application range 25 °C–100 °C, one of the key objectives of this work.). In order to choose a suitable form for the thermal softening function $h(T)$, three forms were initially compared as shown in Fig. 14: Linear (Eq. (B.11)), Power Law 1 (Eq. (B.12)), and Johnson–Cook (Eq. (B.14)). As shown in Fig. 14, and not unexpectedly, there is no significant difference in the accuracy of the fits of these three laws over the small temperature range tested. The Linear model (Eq. (B.11)) was chosen for the current work as perhaps the more common and simpler choice, but no advantage is implied. For application over a larger temperature range or for other materials, presumably one of the forms shown in Appendix B would provide a measurable advantage over the others and thus could be adopted.

With the form of the thermal function determined, the eight optimal coefficients ($\alpha_1, \alpha_2, H_{HV}, n_{HV}, V_{HV}, A_{HV}, B_{HV}, \beta$) may be determined for the combined function, again using results from the three tensile tests (at three temperatures) for each material:

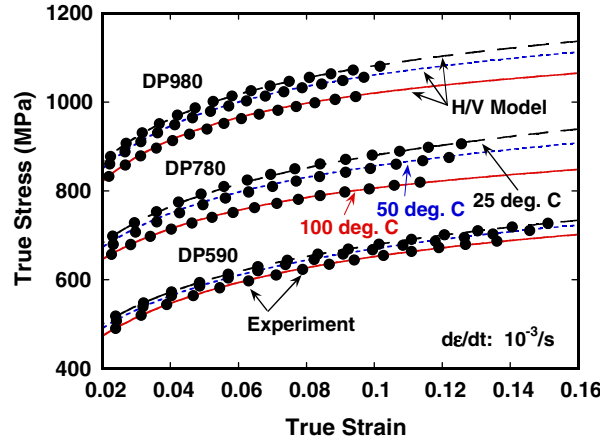


Fig. 13. Comparison of isothermal tensile test data and best-fit H/V model for DP590, DP780, and DP980.

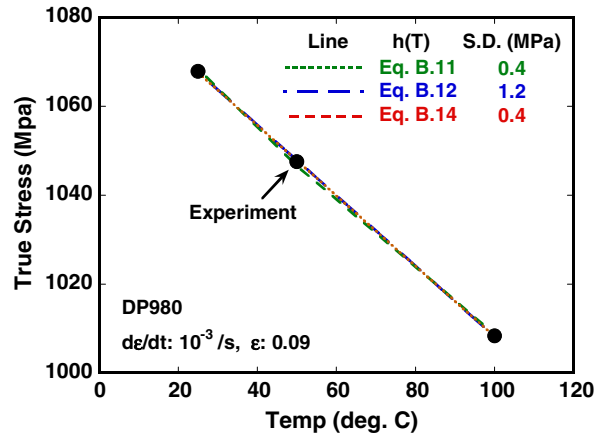


Fig. 14. Comparison of temperature dependent functions $h(T)$ for DP980.

$$f(\epsilon, T) \cdot h(T) = [\alpha(T)(H_{HV}\epsilon^{n_{HV}}) + (1 - \alpha(T))V_{HV}(1 - A_{HV}e^{-B_{HV}\epsilon})] \cdot [1 - \beta(T - T_0)] \quad (12)$$

Using the method of least squares, high and low values of each variable were selected as initial values, producing 2^8 sets of starting sets of parameters. The approximate range of parameters were known with Hollomon and Voce fit with the material data, therefore the initial values of each parameter were selected based on the range. If fit values are out of the range, new initial values were selected and fit again. The initial values are shown in the Table 5. Best-fit coefficients were found for each starting set when the absolute value of the difference between the norm of the residuals (square root of the sum of squares of the residuals), from one iteration to the next, was less than 0.001. The set exhibiting the minimum R^2 value was chosen as optimal, as reported in Table 5. The accuracy of the fit is shown in Table 5 as a standard deviation between experiment and fit line and illustrated graphically in Fig. 13.

Using identical procedures, except for the RK model which was fit according to a procedure recommended by provided by its originators (Rusinek, 2009), several alternative constitutive models were fit to the same tensile test and jump test data, as follows:

1. H/V model with $\alpha = 1$ (Hollomon strain hardening at all temperatures).
2. H/V model with $\alpha = 0$ (Voce strain hardening at all temperatures).
3. H/V model with best-fit constant $\alpha = \alpha_o$ (H/V strain hardening, independent of temperature).
4. Lin–Wagoner (LW) model (Eq. (A.7)) (Voce hardening dependent on temperature).
5. Rusinek–Klepaczko (RK) model (Eq. (A.10), (A.11)) (Power-law hardening dependent on temperature).

These choices were made to be representative of the major classes of constitutive models, as reviewed in Section 1.2. Models 1 and 2 are power-law and saturation hardening models, respectively, that are independent of temperature (except for a multiplicative function to adjust flow stress with temperature). Models 3 and 4 allow strain hardening rates to vary with temperature within the frameworks of saturation/Voce or power-law/Hollomon forms, respectively.

Table 5

Trial and best-fit coefficients of the H/V model.

	Trial values			f_H	f_V	Temp. const.	R^2
	Parameters	Low	High				
DP590	H_{HV}	500	1500	H_{HV} : 1051	V_{HV} : 643.9	α_1 : 0.818	0.999 S.D. = 0.5
	n_{HV}	0.05	0.25	n_{HV} : 0.179	A_{HV} : 0.576	α_2 : 0.00193	
	V_{HV}	500	1500		B_{HV} : 22.44	β : 2.7×10^{-4}	
	A_{HV}	0.1	0.6				
	B_{HV}	10	40				
	α_1	0.1	0.9				
	α_2	0	0.005				
	β	0	0.005				
DP780	H_{HV}	500	2000	H_{HV} : 1655	V_{HV} : 752.1	α_1 : 0.507	0.998 S.D. = 2.5
	n_{HV}	0.05	0.25	n_{HV} : 0.213	A_{HV} : 0.265	α_2 : 0.00187	
	V_{HV}	500	1500		B_{HV} : 30.31	β : 5.8×10^{-4}	
	A_{HV}	0.1	0.6				
	B_{HV}	10	40				
	α_1	0.1	0.9				
	α_2	0	0.005				
	β	0	0.005				
DP980	H_{HV}	500	2000	H_{HV} : 1722	V_{HV} : 908.1	α_1 : 0.586	0.999 S.D. = 0.6
	n_{HV}	0.05	0.25	n_{HV} : 0.154	A_{HV} : 0.376	α_2 : 0.00149	
	V_{HV}	500	1500		B_{HV} : 39.64	β : 3.9×10^{-4}	
	A_{HV}	0.1	0.6				
	B_{HV}	10	40				
	α_1	0.1	0.9				
	α_2	0	0.005				
	β	0	0.005				

The material parameters for the RK model, Eq. (A.10), were found using a procedure consisting of six steps recommended by the first author (Rusinek, 2009). Some fundamental constants in RK model: maximum strain rate, minimum strain rate and melting temperature were first to be taken from the literature (Larour et al., 2007) and the elastic modulus was taken to be constant because this study only covered the small homologous temperature range. The remaining six steps followed for fitting the RK model are as follows:

Step 1: $\sigma^*(\dot{\epsilon}_p, T)$ in Eq. (A.11) is zero at low strain rate and at critical temperature. In this study $\sigma^*(\dot{\epsilon}_p, T) = 0$ at the strain rate of $10^{-4}/s$ and the temperature of 300 K since those were the lowest values for strain rate and temperature in this work. Using this strain rate and temperature combination, C1 was calculated.

Step 2: Eq. (A.10) was fit to material data at the strain rate of $10^{-4}/s$ and temperature of 300 K, in which $\sigma^*(\dot{\epsilon}_p, T) = 0$, thus allowing determination of A (10^{-4} , 300 K) and n (10^{-4} , 300 K).

Step 3: The strain rate sensitivity term, $\sigma^*(\dot{\epsilon}_p, T)$, was fit to jump test results in order to determine C0 and m .

Step 4: $A_{ij}(\dot{\epsilon}_i, T_j)$ and $n_{ij}(\dot{\epsilon}_i, T_j)$ were found at each strain rate and temperature using Eq. (A.10).

Step 5: $A(\dot{\epsilon}, T)$ was fit to A_{ij} values to find A0 and A1.

Step 6: $n(\dot{\epsilon}, T)$ was fit to n_{ij} values to find B0 and B1.

The optimal fit coefficients, standard deviations, and R^2 values of all models are shown in Tables 6 and 7.

The true stress–strain curves for each of these fits for DP780 are shown in Fig. 15. While the differences are small in the uniform tensile range (consistent with the small standard errors of fit shown in Tables 5–7), the differences become apparent when extrapolated to higher strains. Strain hardening at strains beyond the tensile uniform range is particularly important for sheet forming applications with high curvature bending, where bending strains can be large. The transition of strain hardening type of the H/V law from more Hollomon-like at room temperature to progressively more Voce-like behavior at 50 and 100 °C can be seen by comparing Figures 13a, 13b and 13c.

Tables 5–7 show that the H/V model provided the lowest standard deviations of fit for each material, followed progressively by the three H/V models with constant α , the LW model, and then the RK model. The difficulty of fitting RK model to the DP steel data has a fundamental origin: the data showed the strain hardening increases with increasing strain rate but decreases with increasing temperature, while the RK model requires that the effects of increasing strain rate and temperature have the same sign of effect on the strain hardening rate.

4.2. Comparison of constitutive model predictions with hydraulic bulge tests

Fig. 16 compares the various constitutive models established above from tensile data with results from room-temperature (25 °C) hydraulic bulge tests. It is apparent visually and from the standard deviations computed over the strain range

Table 6
Best-fit coefficients of H/V model for $\alpha(T) = 1$, $\alpha(T) = 0$, and $\alpha(T) = \alpha_0$.

	$\alpha(T) = 1^a$		$\alpha(T) = \alpha_0^b$		$\alpha(T) = 0^a$	
	$f(\epsilon)h(T)$	R^2 S.D.(MPa)	$f(\epsilon)h(T)$	R^2 S.D.(MPa)	$f(\epsilon)h(T)$	R^2 S.D.(MPa)
DP590	H_1 : 1039 n_1 : 0.186 β : 5.4×10^{-4}	0.998 S.D. = 2.5	α_0 : 0.875 H_1 : 983 n_1 : 0.166 V_0 : 806.9 A_0 : 0.825 B_0 : 22.4 β : 5.5×10^{-4}	0.999 S.D. = 0.9	V_0 : 761.45 A_0 : 0.452 B_0 : 14.6 β : 5.6×10^{-4}	0.999 S.D. = 2.0
DP780	H_1 : 1234 n_1 : 0.148 β : 1.0×10^{-3}	0.997 S.D. = 3.2	α_0 : 0.850 H_1 : 1147 n_1 : 0.175 V_0 : 1521 A_0 : 0.289 B_0 : 37.7 β : 1.0×10^{-3}	0.997 S.D. = 2.8	V_0 : 940.9 A_0 : 0.370 B_0 : 17.19 β : 1.0×10^{-3}	0.997 S.D. = 3.2
DP980	H_1 : 1486 n_1 : 0.135 β : 7.4×10^{-4}	0.996 S.D. = 3.9	α_0 : 0.707 H_1 : 1332 n_1 : 0.125 V_0 : 2154 A_0 : 0.9 B_0 : 52.3 β : 7.4×10^{-4}	0.999 S.D. = 1.3	V_0 : 1111 A_0 : 0.353 B_0 : 24.33 β : 7.4×10^{-4}	0.997 S.D. = 3.2

^a For $\alpha(T) = 1$ and $\alpha(T) = 0$, the same initial values in Table 5 were used.

^b For $\alpha(T) = \alpha_0$, the same initial values in Table 5 were used except V_0 , A_0 and B_0 which were found out of the range. For these three parameters, 500 and 2500 MPa, 0.1 and 0.9, and 10 and 60 were used for initial values, respectively.

Table 7
Trial and best-fit coefficients of LW and RK models.

	LW			RK		
	Trial Values	$f(\epsilon)h(T)$	R^2 S.D. (MPa)	$f(\epsilon)h(T)$		S.D.(MPa)
DP590	A : 500, 1500 B : 0.1, 0.6 C_1 : -5, -40 C_2 : -0.2, 0 β : -0.9, -0.1	A : 764.5 B : 0.452 C_1 : -14.3 C_2 : -0.010 β : -0.229	0.999 S.D. = 2.5	A_0 : 1072 A_1 : 0.076 ϵ_0 : 0 B_0 : 0.184 B_1 : -0.043 C_0 : 180.6 C_1 : 0.53 m : 1.53 A_0 : 1381 A_1 : 0.245	T_m : 1750 K $\dot{\epsilon}_{max}$: $10^7/s$ $\dot{\epsilon}_{min}$: $10^{-5}/s$	S.D. = 4.2
DP780	A : 500, 1500 B : 0.1, 0.6 C_1 : -5, -40 C_2 : -0.2, 0 β : -0.9, -0.1	A : 960.4 B : 0.375 C_1 : -15.2 C_2 : -0.102 β : -0.609	0.998 S.D. = 2.7	ϵ_0 : 0 B_0 : 0.146 B_1 : -0.033 C_0 : 404.3 C_1 : 0.53 m : 2.11	T_m : 1750 K $\dot{\epsilon}_{max}$: $10^7/s$ $\dot{\epsilon}_{min}$: $10^{-5}/s$	S.D. = 9.9
DP980	A : 500, 1500 B : 0.1, 0.6 C_1 : -5, -40 C_2 : -0.2, 0 β : -0.9, -0.1	A : 1118 B : 0.353 C_1 : -23.3 C_2 : -0.032 β : -0.311	0.999 S.D. = 1.8	A_0 : 1575 A_1 : 0.140 ϵ_0 : 0 B_0 : 0.134 B_1 : -0.025 C_0 : 289.6 C_1 : 0.53 m : 1.92	T_m : 1750 K $\dot{\epsilon}_{max}$: $10^7/s$ $\dot{\epsilon}_{min}$: $10^{-5}/s$	S.D. = 10

0.03–0.7, 0.03–0.34, and 0.03–0.23 for DP590, DP780 and DP980, respectively, that the full H/V model and H/V model with the best-fit constant α_0 value (independent of temperature) extrapolated to higher strains reproduce the hydraulic bulge test results with much greater fidelity than either Hollomon or Voce hardening models. Note that the experimental stress–strain

behavior for these materials is intermediate between standard Voce and Hollomon laws, and further that the H/V law fit from the tensile predicts the high-strain behavior much better than the standard ones. This result illustrates the achievement of one of the principal objectives of the current development predicting large strain, stress–strain curves accurately. It would be desirable to have data like that shown in Fig. 16 at other temperatures. Unfortunately, the authors are unaware of any facility capable of elevated temperature balanced biaxial testing of high strength steels.

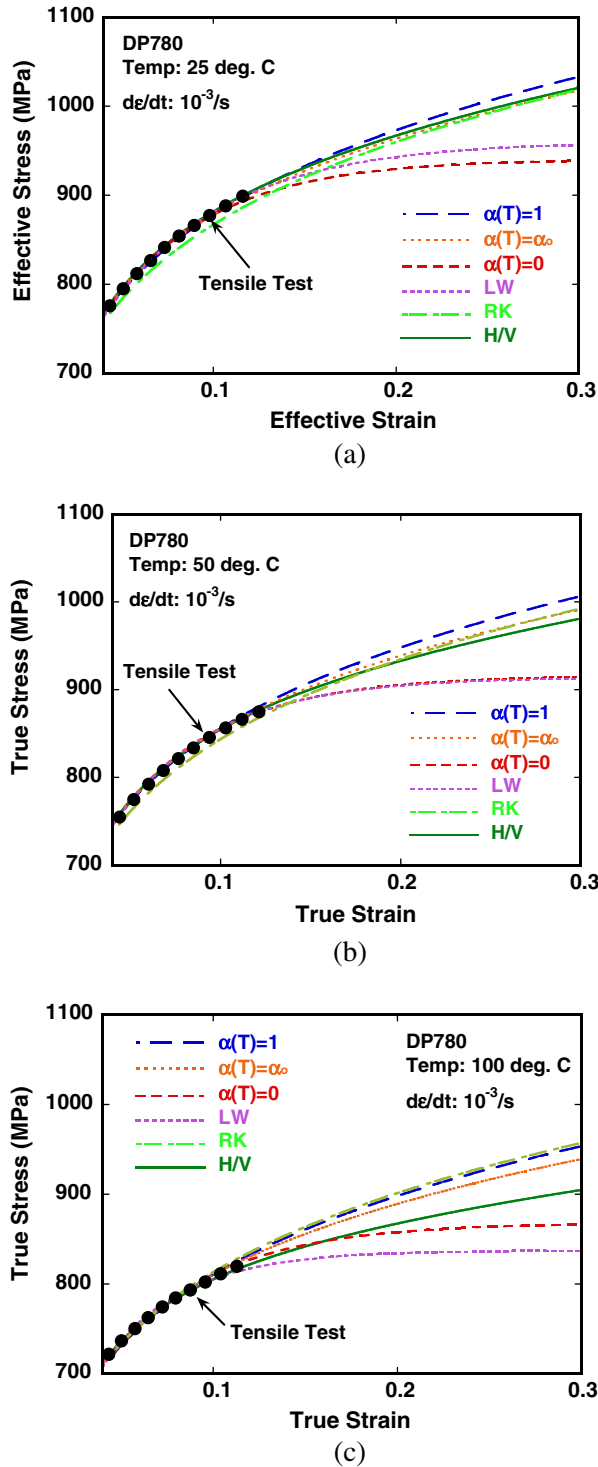
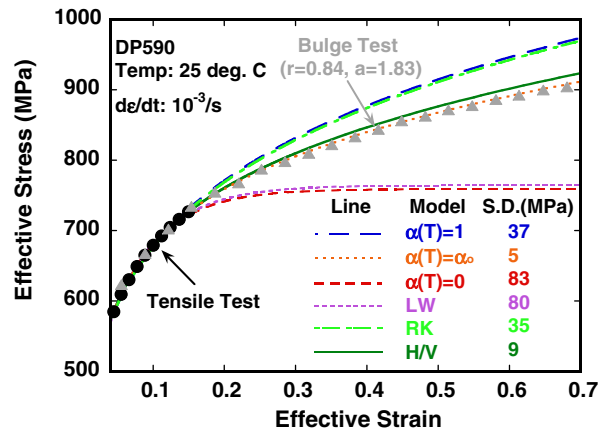


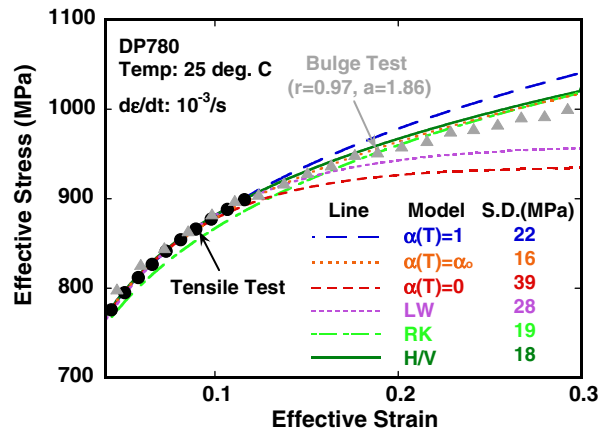
Fig. 15. Comparison of selected constitutive models at various temperatures, DP780: (a) 25 °C, (b) 50 °C and (c) 100 °C.

4.3. Comparison of H/V model predictions with tensile tests to failure

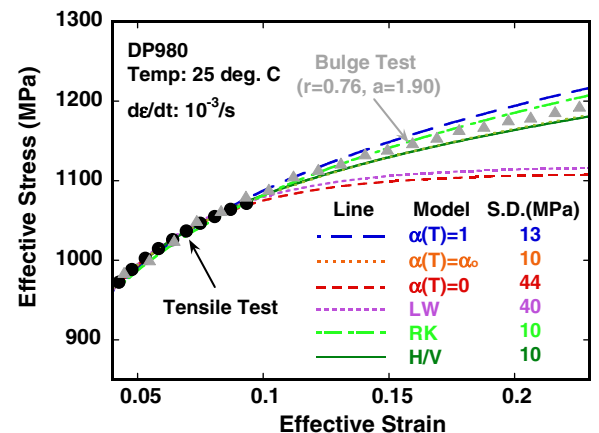
In order to assess the accuracy and usefulness of the proposed constitutive model on plastic localization and failure, three kinds of tensile tests to failure were simulated using finite element procedures described in Sections 3.6 and 3.7. For the first set of tests, standard non-isothermal tensile tests were conducted in air at room temperature at a nominal strain rate of



(a)



(b)



(c)

Fig. 16. Comparison of constitutive models with bulge test results: (a) DP590, (b) DP780 and, (c) DP980.

$10^{-3}/s$ (at the rate to which the model coefficients were fit), and were compared with thermo-mechanical FE simulations using selected constitutive models. The results, Fig. 17(a) shows that the H/V model predicts post-uniform straining accurately as compared with other models, for all three materials. The average percentage error between the measured and simulated elongation to failure, e_f , is 3% for the H/V model vs. 16% for the Hollomon ($\alpha = 1$) law, 25% for the Voce ($\alpha = 0$) law, 5% for $\alpha(T) = \alpha_0$, 21% for LW and 33% for RK.

Similar tensile tests were conducted at strain rate of $1/s$ (the maximum strain rate available to the authors). Fig. 17(b) confirms that the H/V model predicts well the ultimate tensile strength as well as total elongation for all three DP steels at the highest rate for which tests were available, well outside of the fit range of rates.

For the third kind of assessment of strain localization and failure, tensile tests were conducted isothermally at three temperatures, 25, 50, and 100 °C, and were simulated using isothermal FEM. That is, the temperature was maintained at the initial temperature throughout the simulation and test. The isothermal tests and simulations using various laws are compared in Fig. 18 for one material, DP590, and the corresponding differences of total elongation obtained. A summary of combined errors for each law and each material over all three temperatures appears in Table 8. The H/V model predicts the development of post-uniform necking over a range of temperatures with much better accuracy than other such models, typically better by an order of magnitude.

Fig. 19 shows the simulated differences of post-uniform straining for isothermal and non-isothermal tests. As expected, the differences at a nominal strain rate of $10^{-3}/s$ are small because there is sufficient heat flow to approximate isothermal condition. For the simulated tests conducted at a nominal strain rate of $10/s$, the effect of deformation-induced heating is greater because the heat flow is restricted for the shorter test time, thus approaching adiabatic conditions. The standard deviations for H/V predictions are factors of 2–8 less than those for the other models.

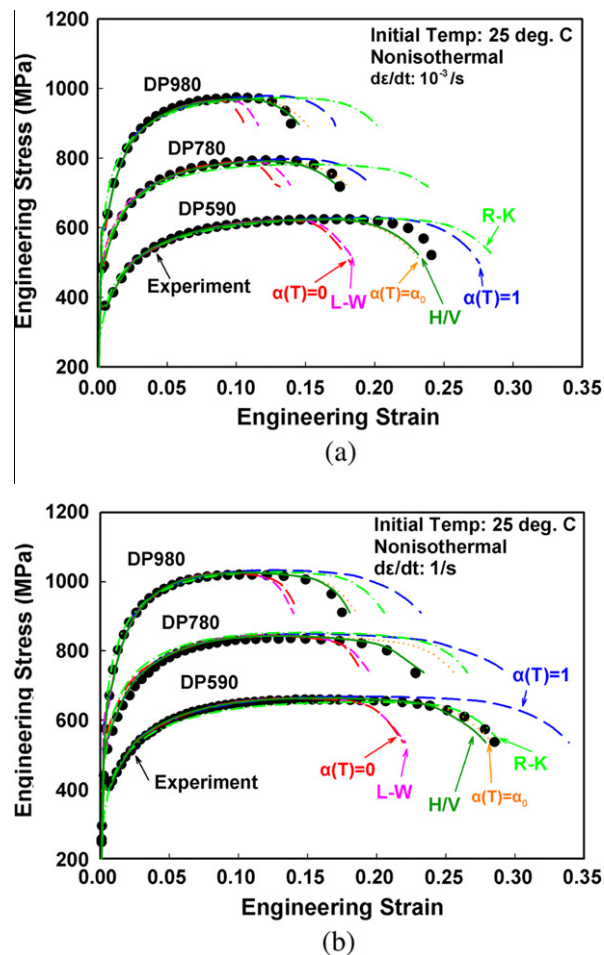
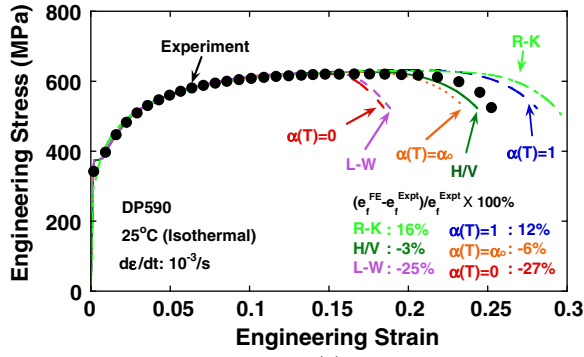
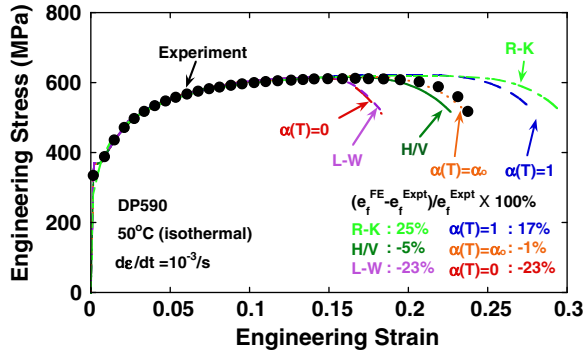


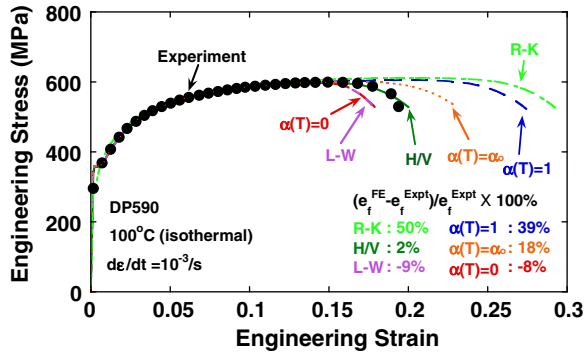
Fig. 17. Comparison of nonisothermal tensile test data and FE simulation using selected constitutive models: (a) at strain rate = $10^{-3}/s$ and (b) at strain rate = $1/s$.



(a)



(b)



(c)

Fig. 18. Comparison of isothermal tensile test data and FE simulation using selected constitutive models for DP590: (a) at 25 °C, (b) at 50 °C and (c) at 100 °C.

Table 8

Difference ^a of total elongations of isothermal tensile tests conducted at 25, 50, and 100 °C and FE simulations for various constitutive models.

	LW (%)	RK (%)	$\alpha(T) = 1$ (%)	$\alpha(T) = 0$ (%)	$\alpha(T) = \alpha_0$	H/V (%)
DP590	19	30	23	19	8	3
DP780	21	47	21	22	11	5
DP980	18	50	29	23	13	6
Avg.	19	42	24	21	11	5

^a The percentage error of predicted failure elongation is computed by $(e_{f,FE} - e_{f,exp})/e_{f,exp} \times 100(\%)$ where $e_{f,FE}$ is the predicted elongation at the time step when the predicted load matches the measured load at $e_{f,exp}$. The percentage error shown in the table is the average of the absolute values of these percentage errors for three temperatures: 25, 50, and 100 °C.

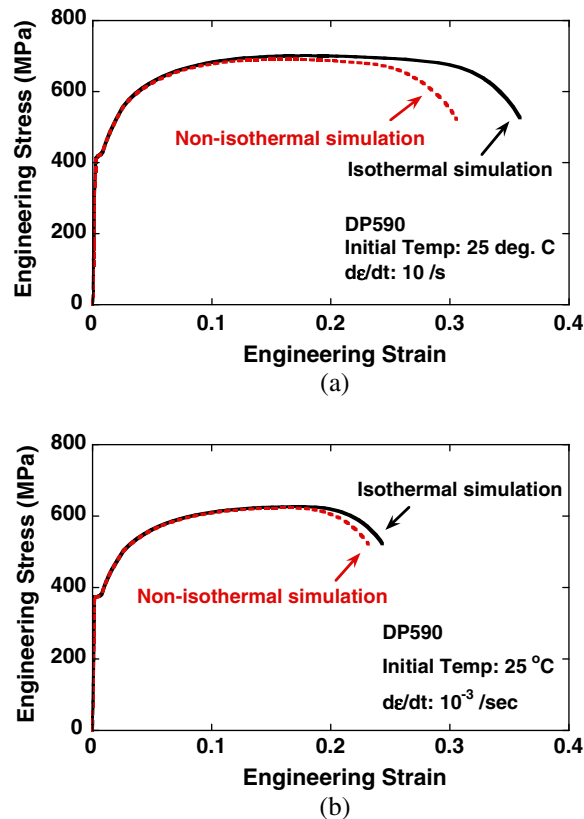


Fig. 19. Comparison of isothermal and non-isothermal FE simulations of tensile test using the H/V model at two nominal strain rates: (a) 10/s and (b) 10^{-3} /s.

5. Summary and conclusions

Standard jump tests and isothermal tensile tests of DP590, DP780 and DP980 steels in the uniform strain range at 25, 50 and 100 °C have been used to fit constitutive equations from the literature and as proposed in the current work (“H/V Model”). The accuracy of these laws was compared using tensile tests to failure (isothermal and standard) and balanced biaxial bulge tests, and parallel simulations. The following conclusions were reached:

1. The H/V Model provides a natural form to incorporate the transition of strain hardening from power-law-type (Hollomon-like) at low homologous temperatures (and for many bcc alloys) to saturation-type (Voce-like) at higher homologous temperatures (and for many bcc alloys).

2. The H/V Model, fit to the uniform strain range of tensile data, provides more accurate predictions of large-strain stress-strain behavior than existing models in the literature.

3. The H/V Model, fit to the uniform strain range of tensile data, predicts tensile failure strains more accurately, by factors of 2–8, than existing models in the literature.

4. Deformation-induced heating at normal industrial strain rates affects the strain hardening of DP steels significantly, thus promoting strain localization and failure.

5. The accuracy of predicted failure strains and large-strain stress-strain curves using the H/V Model, and the large differences between isothermal and non-isothermal predictions at industrial strain rates, suggest that damage is not a critical factor in the tensile failure of DP steels.

6. The H/V Model can be simplified by setting the linear combination coefficient α equal to a constant: $\alpha = 1$ is a power-law/Hollomon model, $\alpha = 0$ is a saturation/Voce model, and $\alpha = \alpha_0$ exhibits a fixed character intermediate between Hollomon and Voce models. The last simplification provides most of the advantages of the full H/V model over the small range of temperatures investigated in the current work.

7. A heat conversion of efficiency of 0.9 was measured for DP590 steel.

8. Tapered tensile specimens with a 2% taper are sufficient to insure failure at the center for DP steels. Parallel and 1%-tapered specimens are not sufficient.

9. DP steels were found to have varying properties in the edge regions of the coils. The central regions were very uniform. The dividing line between the two regions was measured as 300–360 mm from the coil edge for DP 590 and DP 980 steels having total coil widths of 1500 mm.

10. Many of the common plastic constitutive laws (1-D) incorporating strain, strain rate, and temperature, have been identified and their forms presented. Selected representative ones that incorporate varying strain hardening as a function of temperature have been implemented and compared.

Acknowledgements

This work was supported cooperatively by the National Science Foundation (Grant CMMI 0727641), the Department of Energy (Contract DE-FC26-02OR22910), the Auto/Steel Partnership, and the Transportation Research Endowment Program at the Ohio State University.

We would like to thank Dr. J.W. Yoon and John C. Brem at the Alcoa Technical Center for conducting hydraulic bulge tests, Dr. F. Barlat (Pohang University of Science and Technology) and Dr. Kwansoo Chung (Seoul National University) for discussing on the bulge test results and Dr. J.R. Fekete (GMNA Body Manufacturing Engineering) for acquiring the materials and providing standard tensile tests and arranging for chemical analysis of the same.

Appendix A. Integrated constitutive equations

There are many 1-D integrated constitutive equations proposed. This section lists these equations briefly.

A.1. Brown–Anand model (Anand, 1982, 1985; Brown et al., 1989)

$$\dot{\epsilon}^p = A \exp\left(-\frac{Q}{RT}\right) \left[\sinh\left(B\frac{\sigma}{s}\right)\right]^{1/m} \tag{A.1}$$

$$\text{Evolution equation : } \begin{cases} \dot{s} = \{C(1 - \frac{s}{s^*})\} D_{\text{sign}}(1 - \frac{s}{s^*}) \dot{\epsilon}^p \\ s^* = E \left[\frac{\dot{\epsilon}^p}{A}\right]^f \exp\left(\frac{Q}{RT}\right)^f \end{cases} \tag{A.2}$$

where $\dot{\epsilon}_p$ is the plastic strain rate, s is an internal variable, deformation resistance, R is a gas constant, T is the present temperature (K), and A, B, C, D, E, F, Q , are parameters to be found.

A.2. Mechanical threshold stress (MTS) model (Kocks, 1976; Mecking and Kocks, 1981; Follansbee and Kocks, 1988)

$$\sigma = \sigma_a + (\hat{\sigma} - \sigma_a) \left\{ 1 - \left[\frac{kT}{\mu b^3 g_0} \ln\left(\frac{\dot{\epsilon}_0}{\dot{\epsilon}}\right) \right]^{1/A} \right\}^{1/B} \tag{A.3}$$

$$\text{Evolution equation : } \begin{cases} \frac{d\hat{\sigma}}{d\epsilon} = C \left[1 - \frac{\hat{\sigma} - \sigma_a}{\sigma_s(T, \dot{\epsilon}) - \sigma_a} \right] \\ \ln\left(\frac{\dot{\epsilon}}{\dot{\epsilon}_{s0}}\right) = \frac{\mu b^3 D}{kT} \ln\frac{\sigma_s}{\sigma_{s0}} \end{cases} \tag{A.4}$$

where $\hat{\sigma}$ is an internal variable, the mechanical threshold stress, μ is the shear modulus, b is the magnitude of Burgers vector, k is the Boltzmann constant, T is the present temperature (K), $\dot{\epsilon}$ is the plastic strain rate, $\dot{\epsilon}_0$ is the reference strain rate, σ_s is the saturation stress and $\sigma_a, g_0, A, B, C, D, \dot{\epsilon}_{s0}, \sigma_{s0}$ are parameters to be found.

A.3. Modified Bodner and Partom model (Bodner and Partom, 1975; Chen et al., 2008)

$$\dot{\epsilon}^p = \frac{2}{\sqrt{3}} \left(\frac{\sigma}{|\sigma|}\right) A \exp\left[-\left(\frac{B+1}{2B}\right) \left(\frac{Z \exp(CT^{*\beta})}{\sigma}\right)^{2B}\right] \tag{A.5}$$

$$\begin{cases} Z = Z_1 + (Z_0 - Z_1) \exp\left(-D \frac{\int \sigma d\epsilon^p}{Z_0}\right) \\ T^* = \frac{T - T_0}{T_m - T_0} \end{cases} \tag{A.6}$$

where $\dot{\epsilon}_p$ is the plastic strain rate, T is the present temperature (K), T_m is the melting temperature of the material, T_0 is a reference temperature, and $A, B, C, D, \beta, Z_0, Z_1$ are parameters to be found.

A.4. Lin–Wagoner model (Lin and Wagoner, 1987)

$$\sigma = A \{ 1 - B \exp[(C_1 + C_2(T - T_0)) \dot{\epsilon}] \left(\frac{\dot{\epsilon}}{\dot{\epsilon}_0}\right)^m \left(\frac{T}{T_0}\right)^\beta \} \tag{A.7}$$

where T is the present temperature (K), T_0 is a reference temperature, $\dot{\epsilon}$ is the strain rate, $\dot{\epsilon}_0$ is a reference strain rate, and A, B, C_1, C_2, m, β are material constants.

A.5. Zerilli–Armstrong model (Zerilli and Ronald, 1987)

$$\begin{cases} \text{BCC} : \sigma = A_{\text{BCC}} + B_{\text{BCC}} \exp[-(\beta_1 - \beta_2 \ln \dot{\varepsilon})T] + C_{\text{BCC}} \dot{\varepsilon}^n \\ \text{FCC} : \sigma = A_{\text{FCC}} + (B_{\text{FCC}} + C_{\text{FCC}} \dot{\varepsilon}^n) \exp(-\beta_1 T + \beta_2 T \ln \dot{\varepsilon}) \end{cases} \quad (\text{A.8})$$

where T is the present temperature (K), $\dot{\varepsilon}$ is the strain rate, A_{BCC} , B_{BCC} , C_{BCC} , β_1 , β_2 , n (A_{FCC} , B_{FCC} , C_{FCC} , β_1 , β_2 , n) are parameters to be found.

A.6. Khan–Huang–Liang model (Khan and Huang, 1992; Khan and Liang, 1999; Khan and Zhang, 2000, 2001; Khan et al., 2004; Khan et al., 2007)

$$\sigma = \left\{ A + B \left[\left(1 - \frac{\ln(\dot{\varepsilon}^p)}{\ln \dot{\varepsilon}_{\max}} \right) \right]^{n_1} (\dot{\varepsilon}^p)^{n_0} \right\} \left(\frac{\dot{\varepsilon}^p}{\dot{\varepsilon}_0} \right)^m \left(\frac{T_m - T}{T_m - T_0} \right)^\beta \quad (\text{A.9})$$

where $\dot{\varepsilon}_p$ is the plastic strain rate, $\dot{\varepsilon}_0$ is the reference plastic strain rate, $\dot{\varepsilon}_{\max}$ is a upper limit strain rate, T is the present temperature (K), T_m is the melting temperature of the material, T_0 is a reference temperature, and A , B , n_1 , n_0 , m , β are material constants.

A.7. Rusinek–Klepaczko model (Klepaczko, 1987; Rusinek and Klepaczko, 2001; Rusinek et al., 2007)

$$\sigma = \frac{E(T)}{E_0} [A(\dot{\varepsilon}_p, T)(\varepsilon_0 + \varepsilon)^{n(\dot{\varepsilon}_p, T)} + \sigma^*(\dot{\varepsilon}_p, T)] \quad (\text{A.10})$$

$$\begin{cases} \frac{E(T)}{E_0} = 1 - \frac{T}{T_m} \exp(T_c(1 - \frac{T}{T_m})) \\ A(\dot{\varepsilon}_p, T) = A_0 \left[\frac{T}{T_m} \log \left(\frac{\dot{\varepsilon}_{\max}}{\dot{\varepsilon}_p} \right) \right]^{-A_1} \\ n(\dot{\varepsilon}_p, T) = B_0 \left[1 - B_1 \frac{T}{T_m} \log \left(\frac{\dot{\varepsilon}_p}{\dot{\varepsilon}_{\min}} \right) \right] \\ \sigma^*(\dot{\varepsilon}_p, T) = C_0 \left[1 - C_1 \frac{T}{T_m} \log \left(\frac{\dot{\varepsilon}_{\max}}{\dot{\varepsilon}_p} \right) \right]^m \end{cases} \quad (\text{A.11})$$

where $\dot{\varepsilon}_p$ is the plastic strain rate, T is the present temperature (K), T_m is the melting temperature of the material, T_c is the characteristic homologous temperature, $\dot{\varepsilon}_{\max}$ is the maximum strain rate, $\dot{\varepsilon}_{\min}$ is the minimum strain rate, $\dot{\varepsilon}_p$ is the plastic strain rate, E_0 is the young's modulus at 0 K, and ε_0 , T_c , A_0 , A_1 , B_0 , B_1 , C_0 , C_1 , m are parameters to be found.

Appendix B. Composite functions

This section covers the strain hardening, strain rate sensitivity, and thermal softening functions.

B.1. Strain hardening functions: $f(\varepsilon)$

$$(1) \text{ Hollomon, 1945} : \sigma = K\varepsilon^n \quad (\text{B.1})$$

$$(2) \text{ Swift, 1952} : \sigma = K(\varepsilon + \varepsilon_0)^n \quad (\text{B.2})$$

$$(3) \text{ Ludwik, 1909} : \sigma = \sigma_0 + K\varepsilon^n \quad (\text{B.3})$$

$$(4) \text{ Hartley and Srinivasan, 1983} : \sigma = \sigma_0 + K(\varepsilon + \varepsilon_0)^n \quad (\text{B.4})$$

$$(5) \text{ Ludwigson, 1971} : \sigma = K_1 \varepsilon^{n_1} + \exp(K_2 + n_2 \varepsilon) \quad (\text{B.5})$$

$$(6) \text{ Baragar, 1987} : \sigma = \sigma_0 + c\varepsilon^{0.4} + d\varepsilon^{0.8} + e\varepsilon^{1.2} \quad (\text{B.6})$$

$$(7) \text{ Voce, 1948} : \sigma = \sigma_0(1 - A \exp(B\varepsilon)) \quad (\text{B.7})$$

B.2. Strain rate sensitivity functions: $g(\dot{\varepsilon})$

(1) Power law model (Kleemola and Ranta-Eskola, 1979; Hosford and Caddell, 1983)

$$\sigma = \sigma_{\dot{\varepsilon}_0} \left(\frac{\dot{\varepsilon}}{\dot{\varepsilon}_0} \right)^m \quad (\text{B.8})$$

(2) Johnson-Cook model (Johnson and Cook, 1983)

$$\sigma = \sigma_{\dot{\epsilon}_0} \left[1 + m \ln \left(\frac{\dot{\epsilon}}{\dot{\epsilon}_0} \right) \right] \quad (\text{B.9})$$

(3) Wagoner model (Wagoner, 1981a)

$$\sigma = \sigma_{\dot{\epsilon}_0} \left(\frac{\dot{\epsilon}}{\dot{\epsilon}_0} \right)^{m_0 \sqrt{\dot{\epsilon}/\dot{\epsilon}_0}^{m_1}} \quad (\text{B.10})$$

B.3. Thermal softening functions: $h(T)$

(1) Linear model (Hutchison, 1963)

$$h(T) = \sigma_{\text{iso}} (1 - \beta(T - T_r)) \quad (\text{B.11})$$

(2) Power law model 1 (Zuzin et al., 1964; Misaka and Yoshimoto, 1969)

$$h(T) = \sigma_{\text{iso}} \left(\frac{T}{T_0} \right)^\beta \quad (\text{B.12})$$

(3) Power law model 2 (Lubahn and Schnectady, 1947)

$$h(T) = \sigma_{\text{iso}} (a)^{\frac{T}{T_m}} \quad (\text{B.13})$$

(4) Johnson-Cook model (1983)

$$h(T) = \sigma_{\text{iso}} \left[1 - \left(\frac{T - T_0}{T_m - T_0} \right)^\beta \right] \quad (\text{B.14})$$

(5) Khan model (Khan et al., 2004)

$$h(T) = \sigma_{\text{iso}} \left(\frac{T_m - T}{T_m - T_0} \right)^\beta \quad (\text{B.15})$$

(6) Exponential model 1 (Wada et al., 1978)

$$h(T) = \sigma_{\text{iso}} \exp \left(\frac{A}{BT} \right) \quad (\text{B.16})$$

(7) Exponential model 2 (Chen et al., 2008)

$$h(T) = \sigma_{\text{iso}} \exp \left(C \left(\frac{T - T_0}{T_m - T_0} \right)^m \right) \quad (\text{B.17})$$

References

- ABAQUS, 2007. Abaqus user's manual for version 6.7, Hibbit, Karlson & Sorensen Inc.
- Anand, L., 1982. Constitutive equations for the rate-dependent deformation of metals at elevated temperatures. *Journal of Engineering Materials and Technology* 104, 12–17.
- Anand, L., 1985. Constitutive equations for hot working of metals. *International Journal of Plasticity* 1, 213–231.
- ATC, 2008. 100 Technical Lane, New Kensington, PA.
- Ayres, R.A., 1985. Thermal gradients, strain rate, and ductility in sheet steel tensile specimens. *Metallurgical and Materials Transaction A* 16A, 37–43.
- Baragar, D.L., 1987. The high temperature and high strain-rate behavior of a plain carbon and an HSLA steel. *Journal of Mechanical Working Technology* 14, 295–307.
- Bodner, S.R., Partom, Y., 1975. Constitutive equations for elastic–viscoplastic strain-hardening materials. *Journal of Applied Mechanics* 46, 805–810.

- Boger, R.K., Wagoner, R.H., Barlat, F., Lee, M.G., Chung, K., 2005. Continuous, large strain, tension/compression testing of sheet material. *International Journal of Plasticity* 21, 2319–2343.
- Brem, J.C., 2008. Mechanical behavior characterizations-steel sheet.
- Brown, S.B., Kim, K.H., Anand, L., 1989. An internal variable constitutive model for hot working of metals. *International Journal of Plasticity* 5, 95–130.
- Burte, P.R., Im, Y.T., Altan, T., Semiatin, S.L., 1990. Measurement and analysis of the heat transfer and friction during hot forging. *Journal of Engineering for Industry* 112, 332–339.
- Chen, S., Huang, C., Wang, C., Duan, Z., 2008. Mechanical properties and constitutive relationships of 30CrMnSiA steel heated at high rate. *Materials Science and Engineering A*, 105–108.
- Chen, X.M., DU, C., Wu, X., Zhu, X., Liu, S.-D., 2009. Sheet metal shearing and edge characterization of dual phase steels. *International Deep Drawing Research Group, Golden, USA*, pp. 809–823.
- Choudhary, B.K., Isaac, S.E., Bhanu, S.R.K., Mannan, S.L., 2001. Tensile stress-strain and work hardening behavior of 316LN austenitic stainless steel. *Materials Science and Technology* 17, 223–231.
- Fekete, J., 2009. Private communication, 30001 Van Dyke Ave., Warren, MI, USA.
- Follansbee, P.S., Kocks, U.F., 1988. A constitutive description of the deformation of copper based on the use of the mechanical threshold stress as an internal state variable. *Acta Metall.* 36, 81–93.
- Gao, Y., Wagoner, R.H., 1987. A simplified model of heat generation during the uniaxial tensile test. *Metallurgical and Materials Transaction A* 18A, 1001–1009.
- Ghosh, A.K. (Ed.), 2006. *ASM Handbook, Metalworking: Sheet Forming*. ASM International, Materials Park, OH, USA, pp. 709–732.
- GMNA, 2007. *GMNA Materials Lab*, 660 South Blvd., Pontiac, MI, USA.
- Hartley, C.S., Srinivasan, R., 1983. Constitutive equations for large plastic deformation of metals. *Journal of Engineering Materials and Technology* 105, 162–167.
- Hill, R., 1979. *Theoretical Plasticity of Textured Aggregates*. The Cambridge Philosophical Society, pp. 179–191.
- Hollomon, J.H., 1945. Tensile deformation. *Transactions of AIME* 162, 268–290.
- Horstemeyer, M.F., Matalanis, M.M., Sieber, A.M., Botos, M.L., 2000. Micromechanical finite element calculations of temperature and void configuration effects on void growth and coalescence. *International Journal of Plasticity* 16, 979–1015.
- Hosford, W.F., Caddell, R.M., 1983. *Metal Forming: Mechanics and Metallurgy*. Prentice-Hall International, Inc., Englewood Cliffs, NJ.
- Huang, M., Zhang, L., Yang, L., 2008. On the failure of AHSS at tooling radius. *Numisheet 2008*, 307–309.
- Hutchison, M.M., 1963. The temperature dependence of the yield stress of polycrystalline iron. *Philosophical Magazine* 8, 121–127.
- Johnson, G.R., Cook, W.H., 1983. A constitutive model and data for metals subjected to large strains, high strain rates and high temperatures. In: *The 7th International Symposium on Ballistic*, p. 541.
- Johnson, G.R., Holmquist, T.J., 1988. Evaluation of cylinder-impact test data for constitutive model constants. *Journal of Applied Mechanics* 64, 3901–3910.
- Khan, A.S., Huang, S., 1992. Experimental and theoretical study of mechanical behavior of 1100 aluminum in the strain rate range 10^{-5} – 10^4 s⁻¹. *International Journal of Plasticity* 8, 397–424.
- Khan, A.S., Kazmi, R., Farrukh, B., 2007. Multiaxial and non-proportional loading responses, anisotropy and modeling of Ti–6Al–4V titanium alloy over wide ranges of strain rates and temperatures. *International Journal of Plasticity* 23, 931–950.
- Khan, A.S., Liang, R., 1999. Behaviors of three BCC metal over a wide range of strain rates and temperatures: experiments and modeling. *International Journal of Plasticity* 15, 1089–1109.
- Khan, A.S., Suh, Y.S., Kazmi, R., 2004. Quasi-static and dynamic loading responses and constitutive modeling of titanium alloys. *International Journal of Plasticity* 20, 2233–2248.
- Khan, A.S., Zhang, H., 2000. Mechanically alloyed nanocrystalline iron and copper mixture: behavior and constitutive modeling over a wide range of strain rates. *International Journal of Plasticity* 16, 1477–1492.
- Khan, A.S., Zhang, H., 2001. Finite deformation of a polymer: experiments and modeling. *International Journal of Plasticity* 17, 1167–1188.
- Kleemola, H.J., Ranta-Eskola, A.J., 1979. Effect of strain rate and deformation temperature on the strain-hardening of sheet steel and brass in uniaxial tension. *Sheet Metal Industry*, 1046–1057.
- Klepaczko, J.R., 1987. A practical stress-strain-strain rate-temperature constitutive relation of the power form. *Journal of Mechanical Working Technology* 15, 143–165.
- Kocks, U.F., 1976. Laws for work-hardening and low-temperature creep. *Transactions of the ASME*, 76–85.
- Kular, G.S., Hillier, M.J., 1972. Re-interpretation of some simple tension and bulge test data for anisotropic metals. *International Journal of Mechanical Sciences* 14, 631–634.
- Larour, P., Rusinek, A., Klepaczko, J.R., Bleck, W., 2007. Effects of strain rate and identification of material constants for three automotive steels. *Steel Research International* 78, 348–357.
- Lee, S.B., Speer, J.G., Matlock, D.K., 2004. The influence of phase distributions and interfaces on fracture and formability of high strength sheet steels. *Advanced High Strength Steels*, 383–394.
- Lin, M.R., Wagoner, R.H., 1986. Effect of temperature, strain, and strain rate on the tensile flow stress of I. F. steel and stainless steel type 310. *Scripta Metallurgica* 20, 143–148.
- Lin, M.R., Wagoner, R.H., 1987. An experimental investigation of deformation induced heating during tensile testing. *Metallurgical and Materials Transactions A* 18A, 1035–1042.
- Lubahn, J.D., Schnechtady, N.Y., 1947. Derivation of stress, strain, temperature, strain-rate relation for plastic deformation. *Journal of Applied Mechanics* 14, A229–230.
- Ludwigson, D.C., 1971. Modified stress-strain relation for FCC metals and alloys. *Metallurgical Transactions* 2, 2825–2828.
- Ludwik, P., 1909. *Element der Technologischen Mechanik*. Springer.
- McVeigh, C., Liu, W.K., 2008. Linking microstructure and properties through a predictive multiresolution continuum. *Computer Methods in Applied Mechanics and Engineering* 197, 3268–3290.
- Mecking, H., Kocks, U.F., 1981. Kinetics of flow and strain-hardening. *Acta Metallurgica* 29, 1865–1875.
- Misaka, Y., Yoshimoto, T., 1969. Formulation of mean resistance of deformation of plain carbon steel at elevated temperature. *Journal of Japan Society Technology Plat* 8, 1967–1968.
- Mishra, N.S., Mishra, S., Ramaswamy, V., 1989. Strain-hardening behavior in high-strength steel. *Metallurgical Transactions* 20A, 2819–2829.
- Ohwue, K., Yoshida, T., Usuda, M., 1992. Influence of material properties and work process factors in sheet metal forming. *Numisheet 1992*, 525–551.
- Piao, K., Lee, J.K., Kim, H.Y., Wagoner, R.H., 2009. Tension/compression test of Mg AZ31B at elevated temperature, 2009 TMS Annual Meeting.
- Raghavan, K.S., Wagoner, R.H., 1987. Combined influence of geometric defects and thermal gradients on tensile ductility. *Metallurgical Transactions* 18A, 2143–2150.
- Ranta-Eskola, A.J., 1979. Use of the hydraulic bulge test in biaxial tensile testing. *International Journal of Mechanical Sciences* 21, 457–465.
- Rusinek, A., 2009. Personal communication, Metz University, 57045 Metz, France.
- Rusinek, A., Klepaczko, J.R., 2001. Shear testing of a sheet steel at wide range of strain rates and a constitutive relation with strain-rate and temperature dependence of the flow stress. *International Journal of Plasticity* 17, 87–115.
- Rusinek, A., Zaera, R., Klepaczko, J.R., 2007. Constitutive relations in 3-D for a wide range of strain rates and temperatures – application to mild steels. *International Journal of Solids and Structures* 44, 5611–5631.
- Sarwar, M., Ahmad, E., Hussain, N., Ahmad, B., Manzoor, T., 2006. Crack path morphology in dual-phase steel. *Journal of Materials Engineering and Performance* 15, 352–354.

- Saxena, A., Chatfield, D.A., 1976. High strain rate behavior of some hot and cold rolled low carbon steels.
- Sente-Software, 2007. JMatPro: Practical software for materials properties. Surney Tech. Center, UK.
- Sklad, M.P., 2008. Analysis of deformation in the shear and shear-tension tests. *Numisheet 2008*, 91–95.
- Sun, D.-Z., Andrieux, F., Feucht, M., 2009. Damage modeling of a TRIP steel for integrated simulation from deep drawing to crash. In: 7th European LS Dyna Conference.
- Swift, H.W., 1952. Plastic instability under plane stress. *Journal of Mechanics Physics of Solids* 1, 1–18.
- Takuda, H., Mori, K., Hatta, N., 1999. The application of some criteria for ductile fracture to the prediction of the forming limit of sheet metals. *Journal of Materials Processing Technology* 95, 116–121.
- Vernerey, F., Liu, W.K., Moran, B., 2007. Multi-scale micromorphic theory for hierarchical materials. *Journal of the Mechanics and Physics of Solids* 55, 2603–2651.
- Voce, E., 1948. The relationship between stress and strain for homogeneous deformation. *Journal of the Institute Metals* 74, 537–562.
- Wada, M., Nakamura, T., Kinoshita, N., 1978. Distribution of temperature, strain rate and strain in plastically deforming metals at high strain rates. *Philosophical Magazine* 38, 167–185.
- Wagoner, R.H., 1980. Measurement and Analysis of Plane-Strain Work Hardening. *Metallurgical Transactions* 11A, 165–175.
- Wagoner, R.H., 1981a. A new description of strain-rate sensitivity. *Scripta Metallurgica* 15, 1135–1137.
- Wagoner, R.H., 1981b. A technique for measuring strain-rate sensitivity. *Metallurgical Transactions* 12A, 71–75.
- Wagoner, R.H., 2006. Advanced high-strength steels: fundamental research issues. In: Wagoner, R.H. (Ed.), Arlington, VA, USA, National Science Foundation, Department of Energy, Auto-Steel Partnership.
- Wagoner, R.H., Chenot, J.L., 1997. *Fundamentals of Metal Forming*. John Wiley & Sons.
- Wagoner, R.H., Kim, Y.H., Keum, Y.T., 1990. 3-D sheet forming analysis including the effects of strain-hardening, rate-sensitivity, anisotropy, friction, heat generation and transfer. *Advanced Technology of Plasticity* 4, 1751–1756.
- Wagoner, R.H., Madeshia, A., Sung, J.H., Kim, J.H., 2009a. Plasticity and failure of advanced high strength steel. *Plasticity*.
- Wagoner, R.H., Sung, J.H., Kim, J.H., 2009b. Unique formability of advanced high strength steels. *Great Design in Steel*.
- Xue, L., 2008. Constitutive modeling of void shearing effect in ductile fracture of porous materials. *Engineering Fracture Mechanics* 75, 3343–3366.
- Young, R.F., Bird, J.E., Duncan, J.L., 1981. An automated hydraulic bulge tester. *Journal of Applied Metalworking* 2, 1–11.
- Zerilli, F.J., Ronald, R.W., 1987. Description of tantalum deformation behavior by dislocation mechanics based constitutive relations. *Journal of Applied Mechanics* 68, 1580–1591.
- Zuzin, W.I., Broman, M.Y., Melnikov, A.F., 1964. Flow resistance of steel at hot forming. *Metallurgy*.